Fabian Muralter, BSc

Preparation and Structure Characterisation of Crystalline Alq(3) in Thin Films

MASTER THESIS

to achieve the university degree of

Diplom-Ingenieur

Master's degree program: Advanced Materials Science

submitted to

Graz University of Technology

Supervisor: Ao. Univ.-Prof. Dr. Roland Resel

Institute of Solid State Physics

Graz, November 2016

AFFIDAVIT

I declare that I have authored this thesis independently, that I have not used other than the declared sources/resources, and that I have explicitly indicated all material which has been quoted either literally or by content from the sources used.
The text document uploaded to TUGRAZonline is identical to the present master‘s thesis.

.....	.....
date	(signature)

Contents

1 Acknowledgements **1**

2 Abstract **2**

3 Kurzfassung **3**

4 Introduction **4**

5 Fundamentals **5**
5.1 Physical and structural properties of Alq(3) 5
5.2 X-ray techniques 7
5.2.1 X-ray reflectivity (XRR) 8
5.2.2 X-ray diffraction (XRD) 9
5.2.3 Grazing incidence X-ray diffraction (GIXD) 10
5.3 Lattice phonon Raman spectroscopy 11

6 Experimental section - sample preparation **13**
6.1 Powder used as the source for evaporation 13
6.2 Evaporation chamber 15
6.3 Evaporation cells 18
6.4 Substrates 24
6.5 Substrate cleaning 25
6.6 Investigation of the substrate surface 26
6.7 Preparation of Alq(3) thin films 29

7 Experimental section - sample investigation **32**
7.1 Optical microscopy 32
7.2 PANalytical Empyrean 36
7.3 X-ray reflectivity (XRR) 37
7.4 Atomic force microscopy (AFM) 43
7.5 Specular X-ray diffraction (XRD) 49
7.6 Grazing incidence X-ray diffraction (GIXD) 51
7.7 Lattice phonon Raman spectroscopy 59

8 Conclusion **65**
8.1 Surface roughness behaviour 65
8.2 Crystallinity of the samples 66
8.3 Challenges in investigation 67

1 Acknowledgements

First, I want to thank my supervisor Roland Resel for giving me the opportunity to work in his group of highly qualified and motivated researchers. This flourished in innumerable fruitful discussions not only with him but with each and every member of this team.
I want to especially thank Stefan Pachmajer, Paul Christian, Harald Spreitzer and Andrew Jones for helping me to get acquainted with the devices in the laboratory.
Furthermore, I want to acknowledge Egbert Zojer and the working group of the project *ThermoLED* that I could be a part of during the past six months. Not only being able to get the support to do the research I've done but also just to be a part of a large academic project has been a great experience for me as a young student.
I also want to thank the *Austrian Research Promotion Agency (FFG)* for financial funding of the whole project.
The research stay in Bologna has been a great opportunity to see another group and their approach to research. I want to acknowledge Tommaso Salzillo and the entire group of Elisabetta Venuti for accepting me and helping me whenever a problem occurred. I would also like to thank the *TU Graz* for granting me the *KUWI fellowship* for the stay in Bologna.
Last, I want to thank my parents and my brother for putting up with me for 23 years now and for keeping me open-minded during my whole course of education.

2 Abstract

Tris-(8-hydroxyquinoline)aluminum (Alq(3)) is an organic molecule that exhibits semiconducting properties. It is used in thin films as an active layer for light-emitting diodes (oLED). Firstly, it has been utilised by Tang and VanSlyke in 1987 to prepare organic LEDs working at low bias voltages. Nowadays, it is still widely used in state-of-the-art organic light-emitting devices. Alq(3) thin films are prepared by physical vapour deposition at different substrate temperatures. Atomic force microscopy reveals that thin films with low surface roughness values of 1 nm are obtained for samples prepared at substrate temperatures close to room temperature. X-ray reflectivity data shows an inhomogeneous but increasing trend of the surface roughness with increasing substrate temperature. It has been shown by grazing incidence X-ray diffraction and lattice phonon Raman spectroscopy that films prepared at substrate temperatures close to room temperature are in an amorphous state. Grazing incidence X-ray diffraction also revealed a preferred orientation of the molecules in the amorphous phase. Inhomogeneous growth of needle-like structures is observed for films prepared at substrate temperatures above 100°C with increasing crystallinity. Large extended crystallites are found when the film has been deposited at substrate temperatures close to the desorption temperature of 170°C. The lattice phonon Raman spectra verified the crystallinity of the needle-like structures which have been shown to correspond to the crystalline α-phase of Alq(3) by grazing incidence X-ray diffraction. These α-phase Alq(3)-crystallites have been evaluated to grow in a preferred orientation on the silicon substrates. Lattice phonon Raman spectra of the α-phase of Alq(3) have been recorded. As the performance of Alq(3)-based LEDs relies crucially on the morphology of the thin films the objective of this work was to prepare samples with different crystallinity of defined phase.

3 Kurzfassung

Tris(8-hydroxychinolin)aluminium (Alq(3)) ist ein organisches Molekül, das mit halbleitenden Eigenschaften vor allem als aktive lumineszente Schicht in Leuchtdioden Anwendung findet. Erstmals wurde es von Tang und VanSlyke 1987 zur Herstellung der ersten organischen Leuchtdioden verwendet. Sonach wurden dessen optische und strukturelle Eigenschaften tiefgehend untersucht, wodurch die Anwendung in modernen Leuchtdioden-Schichtstrukturen ermöglicht wurde. Alq(3)-Dünnfilme wurden mittels physikalischer Gasphasenabscheidung bei unterschiedlicher Substrattemperatur aufgebracht. Untersuchungen mittels Rasterkraftmikroskopie zeigten die geringe Oberflächenrauhigkeit dieser Filme von 1 nm. Ein inhomogenes Verhalten der Oberflächenrauhigkeit als Funktion der Substrattemperatur wurde mittels Röntgenreflektometrie nachgewiesen. Röntendiffraktometrie unter streifendem Einfall und Ramanspektroskopie im Bereich der Gitterphononen wurden verwendet um die amorphe Struktur der Filme hergestellt bei Substrattemperaturen um Raumtemperatur nachzuweisen. Röntgendiffraktometrie unter streifendem Einfall zeigte bevorzugte Orientierung der Alq(3)-Moleküle in der amorphen Phase. Inhomogen wachsende nadelartige Strukturen auf Filmen hergestellt bei Substrattemperaturen über 100°C wurden mit wachsender integraler Kristallinität dieser Filme, untersucht durch Röntendiffraktometrie, in Verbindung gebracht. Ramanspektroskopie im Bereich der Gitterphononen bestätigte die Kristallinität der nadelartigen Strukturen, die durch Röntendiffraktometrie unter streifendem Einfall der kristallinen α-Phase von Alq(3) zugeordnet werden konnte. Bei Substrattemperaturen knapp unter der Desorptionstemperatur von 170°C veränderten mikrometergroße Kristallite auf den Proben deren Oberflächenstruktur. Röntendiffraktometrie unter streifendem Einfall zeigte auch die bevorzugte Orientierung der α-Kristallite auf den Siliziumsubstraten. Ramanspektren im Bereich der Gitterphononen wurden von polykristallinem Pulver der α-Phase von Alq(3) aufgenommen. Die optische Performance Alq(3)-beinhaltender Systeme hängt stark von den strukturellen und phasenanalytischen Eigenschaften der Dünnfilme ab. Daher wurde diese Arbeit benutzt um genau diese Eigenschaften in Abhängigkeit der Substrattemperatur während des Aufdampfprozesses zu untersuchen und Alq(3)-Proben mit unterschiedlicher Kristallinität definierter Phase herzustellen.

4 Introduction

Organic electroluminescent materials have been studied widely in recent decades. A reason for that is the high fluorescence quantum efficiency of a lot of organic materials [1]. As the use of homogeneous films is crucial for the fabrication of oLEDs the application of molecular glasses gets more and more attention. Information on the first organic light emitting diode fabricated by vapour deposition and working at moderate voltage drive has been published by Tang and VanSlyke [1] in 1987. Since then the luminescent material used by that group [1] (namely Alq(3), Tris-(8-hydroxyquinoline)aluminum) has been studied intensively. Structural isomerism, polymorphism and different luminescence spectra connected to these structures are of great scientific interest. Two geometrical isomers exhibiting five different crystal structures have been found [2]. Despite that fact structural analysis of Alq(3) in thin films has not been done as much as the analysis of single crystals. Therefore, just little is known about crystalline structures of Alq(3) in thin films.
Physical vapour deposition has been used by the first group [1] and has been used widely to prepare thin films of Alq(3). So also in this work physical vapour deposition has been chosen as the technique to prepare Alq(3) thin films on silicon/silicon oxide substrates. To investigate structural properties of Alq(3) the substrate temperature during deposition has been varied over a wide range from room temperature up to a point where desorption is dominant and no film will be deposited on the substrate. After preparation of films via physical vapour deposition with different pre-set substrate temperatures the prospect was to get crystalline films at high substrate temperatures. From literature [3] it was known that films deposited at substrate temperatures close to room temperature exhibit amorphous character and desorption will be dominant for temperatures above $\sim$170°C. The higher the temperature the more migration of the impinging molecules will occur on the substrate. As the migrative motion increases deposition at elevated substrate temperatures allows to get structures closer to the thermodynamic equilibrium. This also makes it possible that molecules occupy specific sites that correspond to a crystal structure. Supporting optical microscopy and X-ray reflectivity to get an idea about the morphology of the films two techniques were chosen to investigate the manufactured samples with respect to their crystallinity:

- grazing incidence X-ray diffraction (GIXD) - the integral character
- lattice phonon Raman spectroscopy - more spatially resolved

5 Fundamentals

In this section a short overview about the materials and methods used in the experimental work is given. The fundamental information about the X-ray methods is taken from Birkholz [4], the principles of the Raman technique from Larkin [5]. All the general statements given in the following sections are taken from these books or comprise common knowledge about the techniques and relations described, if not cited otherwise.

5.1 Physical and structural properties of Alq(3)

Alq(3) (Tris-(8-hydroxyquinoline)aluminum) is an organic molecule that consists of an aluminium atom in the center that is bonded to three 8-hydroxyquinoline ligands (see figure 1) [6].

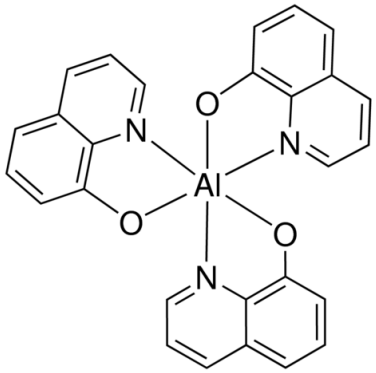

Figure 1: Chemical structure of a Tris-(8-hydroxyquinoline)aluminum (Alq(3)) molecule (drawing taken from [6])

Two different geometrical isomers (see figure 2) are known to crystallise in five crystalline polymorphs (α, β, γ, δ, ϵ) for most of which res- and cif-files are available but the structure of the γ-phase is not fully solved [3] [7] [8] [9] [10] [11] [12] [13] [14]. These phases mostly comprise a close packed arrangement of triangular prisms as which the Alq(3) molecules can be geometrically approximated. The difference between the two isomers is that one of the three 8-hydroxyquinoline ligands is rotated about 180° with respect to this ligand in the other isomer.
Amongst the references listed above Rajeswaran et al. [11] investigated optical properties of the different phases. Samples containing either the meridional or the facial

isomers for example are found to show different luminescence behaviour. These differences are not only caused by the isomers making up the crystals but also by the packing of the crystalline structures themselves [11]. The β- and ϵ-phase were reported to show yellow-green fluorescence and are stated to correspond to the meridional isomer (low temperature isomer - thermodynamically stable at room temperature). The yellow-green fluorescence of the α-phase of Alq(3) amongst other spectroscopic and crystallographic data suggests that this phase also contains Alq(3) molecules of the meridional isomer [11] whereas γ and δ appear to nucleate from the facial isomer (high temperature phases) for which the fluorescence is blue-shifted [2] [11]. Brinkmann et al. [3] describe that the transition between the isomers in solid state happens at $\sim$395°C corresponding to the transition between the α-phase and the γ-phase. In solution the transition between the isomers can occur at lower temperatures (even close to room temperature or below) [9].

To get a quick overview about which isomer crystallises in which polymorph see table 1.

Table 1: Overview of the relation between the Alq(3) isomers and the polymorphs (hypothesis from reference [11])

Isomer	**Polymorph**
Meridional	α, β, ϵ
Facial	γ, δ

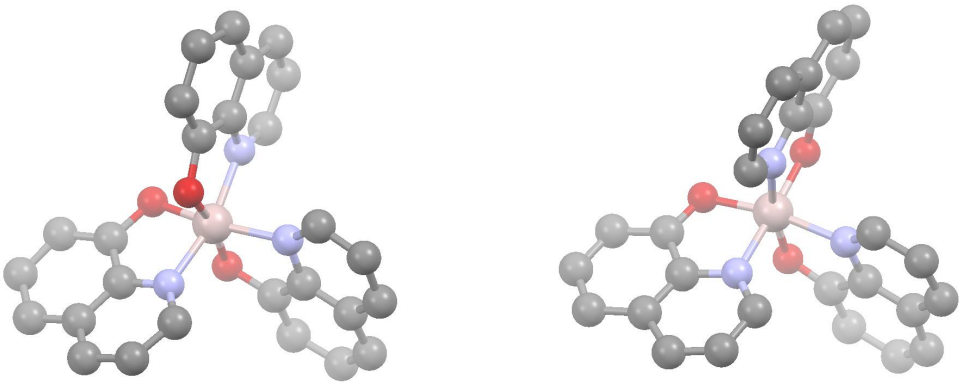

Figure 2: Sketches of the meridional (left) and facial (right) isomer of the Alq(3) molecule drawn with the software *Mercury*

5.2 X-ray techniques

Electromagnetic radiation is used in a variety of different methods to investigate matter. To witness the phenomenon of interference the structures to be investigated need to lie in the region of the wavelength of the used radiation (by rule-of-thumb). In case of crystals of (organic) materials these structures lie in the range of nanometers to Ångströms (10^{-9} m - 10^{-10} m). The electromagnetic radiation exhibiting these wavelengths is called X-ray radiation named by German physicist Wilhelm Röntgen who is credited to have seen fluorescent effects caused by an unknown radiation escaping a type of cathode ray tube first [15].
In a physical lab X-rays are usually generated by an X-ray tube, where electrons (with elementary charge e) are accelerated in vacuum by a high voltage U towards a metal anode. There the fast electrons hit the metal which results in X-ray generation. Here two types of X-ray radiation occur:

- Bremsstrahlung: A continuous spectrum of X-rays up to the maximum kinetic energy of the electrons ($E_{\max} = eU$) is emitted due to scattering and therefore deceleration of the electrons close to the heavy nuclei of the anode material.

- Characteristic X-rays: Electrons that have enough energy can knock out electrons of orbitals close to the nuclei. When those vacancies are then filled up again by electrons occupying higher energy levels X-ray photons can be emitted which are fingerprints for the anode material due to the precise energy differences of these levels.

For crystallographic purposes often copper anodes are used. Mostly the strong pair of Cu K_α-lines is utilised in a convolution of the $K_{\alpha 1}$- and $K_{\alpha 2}$-line in a ratio of 2:1 in diffractometers with a wavelength of $\lambda = 1.5418$ Å [16]. This is also true for the diffractometer described in the experimental section (see section 7.2). Monochromators are used to select one specific line from the whole generated spectrum.
For higher intensities and when monochromatic X-ray radiation of a set energy is required another source can be used - a synchrotron. In a synchrotron charged particles are kept in a circular path by applying electromagnetic fields. These deviations of the straight movement of charged particles cause an emission of radiation (a kind of Bremsstrahlung). This radiation occurs in various wavelengths and therefore a monochromator (crystal) has to be used to select one defined wavelength band (always Gaussian broadening).

5.2.1 X-ray reflectivity (XRR)

X-ray reflectivity (XRR) is a powerful technique pointing an X-ray beam (mostly single characteristic lines from a metal anode) at a "flat" sample at low incident angles. The experiment is performed in specular conditions where the incident and the detected optically reflected beam exhibit equal angles with respect to the surface normal. All three directions lie in one plane (co-planar geometry). Angles around the critical angle of total reflection are examined and the measured intensity curve allows to determine the following properties of the sample investigated:

1. The **film thickness** can be determined from the periodicity of the so called "Kiessig fringes". These fringes are a periodic oscillation of the intensity in the regime at angles above the critical angle of total reflection due to constructive and destructive interference caused by the phase shift coming from reflection of the X-ray beam at the two interfaces of a layer.

2. The **surface/interface roughness** is obtained by the slope of the intensity curve in the angle range where the Kiessig fringes occur. Also the magnitude of the fringes gives information about the surface roughness.

3. The **electron density** can be obtained via the position of the critical angle of total reflection (see equation 2).

The surface roughness σ_{rms} can be evaluated from an XRR measurement (intensity I vs. scattering vector q) with the help of following relation (constant c):

$$I = cq^{-4} \exp\left(q^2 \sigma_{\mathrm{rms}}^2\right) \tag{1}$$

This relation is true for scattering vectors larger than three times the scattering vector q_c corresponding to the critical angle (scattering vector) of total reflection [17].

Simulations in the software *X'Pert Reflectivity* show that a limitation of the method to give reasonable results is that the roughness of a film should not exceed a value of ∼10 % of the film's thickness.

The electron density ρ_e can be evaluated from the position of the critical angle α_c, the wavelength used λ and the classical electron radius $r_e = 2.818 \cdot 10^{-15}$ m [17].

$$\rho_e = \left(\frac{\alpha_c}{\lambda}\right)^2 \cdot \frac{\pi}{r_e} \tag{2}$$

5.2.2 X-ray diffraction (XRD)

As described above in order to see interference phenomena the structures investigated need to be in the range of the wavelength λ of the radiation used. This can be utilised in diffraction experiments where the periodicity in a material can be investigated. Therefore, an X-ray beam is pointed at a sample covering a certain range of incident angles Θ. The detector is then moved correspondingly as the incident and the reflected beam make up an angle of 2Θ to detect specular diffraction. In specular conditions Bragg's law (see equation 3) gives all angles (Θ) where positive interference of the reflected beams and therefore, where intensity maxima (peaks) can be detected for a specific system of repeating planar distances. It can be derived from path differences of reflected beams at two lattice planes with spacing d_{hkl} for a certain lattice plane with Miller indices hkl (see figure 3).

$$\lambda = 2d_{hkl} \sin\left(\frac{2\Theta}{2}\right) \tag{3}$$

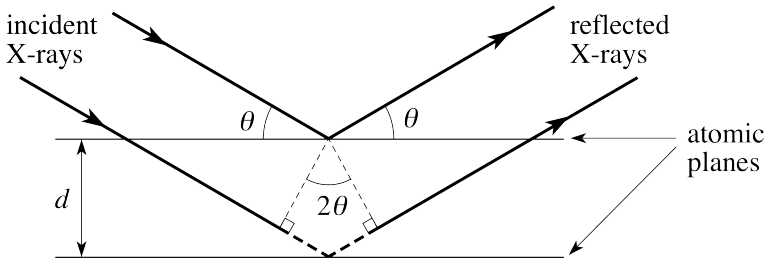

Figure 3: Sketch of a diffraction/interference event at a pair of certain lattice planes (sketch taken from [18])

In a crystalline material one whole crystal can be described by repeating a unit cell in all directions in space. From the scattering on single electrons interference experiments can be described as the scattering on atoms which can be translated onto the whole crystalline material. In this representation the structure factor F is an important property that gives the link between the detected intensity and the positional order of atoms in the unit cell. This allows phase analysis to be performed on the basis of peak positions (2Θ - see equation 3) and peak intensities.

5.2.3 Grazing incidence X-ray diffraction (GIXD)

Grazing incidence X-ray diffraction (GIXD) is a technique where X-ray diffraction (XRD) is performed at low incident angles Θ. The Laue condition (see equation 4) gives all scattering vectors $\vec{q}$ where diffraction will occur (positive interference of reflected X-rays). It states that the scattering vector (difference $\Delta\vec{k}$ between the incident beam $\vec{k}_i$ and the outgoing beam $\vec{k}_o$) needs to be equal to a reciprocal space lattice vector $\vec{G}_{hkl}$ of the investigated system in order to get a diffraction peak.

$$\Delta\vec{k} = \vec{k}_o - \vec{k}_i = \vec{q} = \vec{G}_{hkl} \tag{4}$$

Considering elastic scattering and therefore the wavelength λ to be equal for the incident (direction $\vec{e}_i$) and scattered (direction $\vec{e}_o$) beam the scattering vector $\vec{q}$ can be written as in equation 5.

$$\vec{q} = \frac{2\pi}{\lambda}(\vec{e}_o - \vec{e}_i) \qquad \text{with} \qquad |\vec{q}| = \frac{4\pi}{\lambda}\sin(\frac{2\Theta}{2}) \tag{5}$$

In GIXD measurements additionally to out-of-plane scattering the in-plane part of the scattering vector can also contribute to diffraction which is possible to be detected with 2D-detectors or line-detectors that are moved during the measurement. Knowing the angles and distances in which the detector is positioned enables to calculate an intensity map of the reciprocal space in the detected area. From that the in-plane (q_{xy}) and out-of-plane (q_z) components of the scattering vectors and therefore, the corresponding reciprocal space lattice vectors can be determined.

One distinct peak on the reciprocal space map gives one orientation of a specific Bragg plane. An intensity ring on the other hand corresponds to a Bragg plane not occurring in a preferred orientational order in the sample and therefore, occurring in a "continuous" variety of orientations in the sample.

In general X-ray diffraction is a powerful method to get integral properties of a sample. The data collected in such an experiment provides information about the crystalline structure, the orientation and the order in the investigated system.

5.3 Lattice phonon Raman spectroscopy

Interaction of electromagnetic radiation with matter is not only used in one specific wavelength regime such as X-ray radiation. Raman spectroscopy mostly uses visible or near-infra-red laser light to illuminate a sample and measure the frequency shift (mostly as the Raman shift in wave numbers) between the incoming light and the reflected light. Raman scattering is a form of inelastic scattering where the molecule hit by a photon changes its energy state (see figure 4). Rayleigh scattering (elastic - energy of the incident photon equals the energy of the measured photon) can be observed as the intensity at energy shifts of $\sim$0 cm^{-1} which is filtered out with an interferometric filter in case of the set-up in Bologna. Mostly a shift where the final vibrational state is higher in energy than the initial state is measured via the photon that "loses" the corresponding energy difference (Stokes shift). Vice versa the process where the photon gains energy due to the final state of the molecule being lower in energy than the initial state (anti-Stokes shift) can also be observed but happens at a much lower intensity due to the ground state being much more dominantly occupied at room temperature than states lying higher in energy.

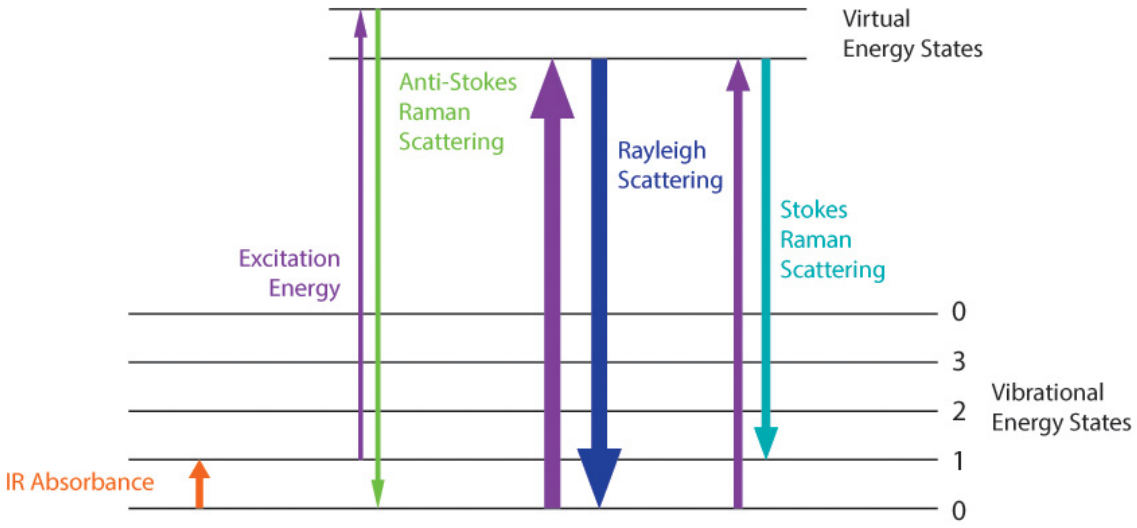

Figure 4: Sketch of different scattering mechanisms on basis of energy levels (sketch taken from [19])

With the help of a microscope a certain area to be investigated can be selected on the sample. As the laser beam and the light for optical observation of the sample run through the same objective not only the area to be investigated but also the volume of the sample to be investigated can be changed. Different focal lengths vary the lateral size of the laser beam but also the depth of focus and therefore, the depth of investigation. In modern micro-Raman systems the zone to be investigated can be reduced down to a few micrometers in all three directions in space [20].

The results from Raman spectroscopy are similar to the results obtained from infra-red spectroscopy (see figure 4). In infra-red spectroscopy mostly the absorption of light that exhibits energies corresponding to resonance of molecular vibrations is measured whereas in Raman spectroscopy the difference between the incident and outgoing photons in energy is recorded.
The detected Raman spectrum of photon energies can then be understood as a representation of a part of the energy landscape of the system in the region (in space and in energy) that has been investigated. This can be used to get information about the intermolecular and intramolecular bonding in the system at hand.

In this work the lattice phonons were the main region of interest. These can be seen at low Raman shifts (up to 150 cm^{-1}) and comprise vibrational and therefore also structural information about the crystalline system investigated [20]. Thus, the lattice phonon Raman spectrum represents a fingerprint of a crystal structure.

6 Experimental section - sample preparation

In the following sections the experimental details about the physical vapour deposition process and the sample preparation are given.

6.1 Powder used as the source for evaporation

The Alq(3) powder used as a source for the physical vapour deposition (PVD) process has been purchased from *Sigma-Aldrich*. Useful properties given by the manufacturer can be found in table 2.

Table 2: Properties of the Alq(3) (Tris(8-hydroxyquinoline)aluminum) powder used as the source for evaporation as given by the manufacturer

Property	**Details**
Manufacturer	Aldrich
Molecular weight	459,43 g/mol
Melting point	>300°C (lit.) / 411°C (DSC)
Purity	99.995 % (sublimed grade)

The polycrystalline powder has been investigated by X-ray powder diffraction (XRPD) on the diffractometer *PANalytical Empyrean* (see section 7.2).

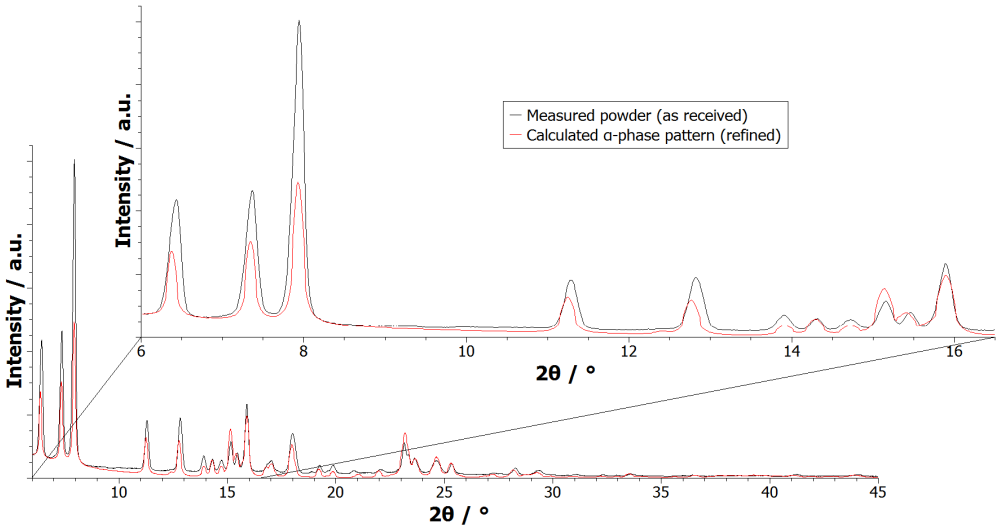

Figure 5: X-ray powder diffraction pattern of the as received Alq(3) (Tris-(8-hydroxyquinoline)aluminum) powder from *Sigma-Aldrich* overlayed with a calculated pattern of the α-phase of Alq(3) (red) [3]; lower plot: whole measured pattern; upper plot: zoom of the 2Θ-range 6° - 20.5°

The diffraction patterns of all the crystalline Alq(3)-phases have been compared to the measured pattern with the help of the software *PowderCell*. As the peak positions of the calculated α-phase and the measured pattern coincide an overlay of these two curves has been plotted and is shown in figure 5. The calculated pattern has been taken from the res-file of Brinkmann et al. [3]. The plot in figure 5 shows that some measured peak positions are slightly shifted with respect to the calculated ones whereas others are exactly at the calculated positions. However, the plot in figure 5 shows also ranges (for example from $2\Theta = 8°$ to $2\Theta = 11°$) where no peaks occur both in the measured and in the calculated pattern. This leads to the conclusion that the powder used for the physical vapour deposition (PVD) process happens to exhibit the α-phase of Alq(3).

6.2 Evaporation chamber

Figure 6 shows a sketch of the vacuum chamber used for the physical vapour deposition (PVD) process. As shown in figure 6 an evaporation cell (see figure 7) is mounted horizontally into the vacuum chamber so that the evaporated molecules "flow" through a tube and hit the sample at a distance of about 30 cm from the cell opening. A hole at the side of the tube allows particles to get to and stick to the quartz microbalance (QMB). The detected shift of the resonance frequency of the quartz crystal is caused by the change of mass that the crystal undergoes due to the impinging molecules sticking to the surface [21]. A shutter is used to control the start and the ending of a deposition process. Knowing the frequency shift of the QMB between those two points in time and measuring the thickness of the sample after the completed deposition process makes it possible to obtain the conversion factor between the frequency shift and the film thickness. This allows for an in-situ thickness monitoring.

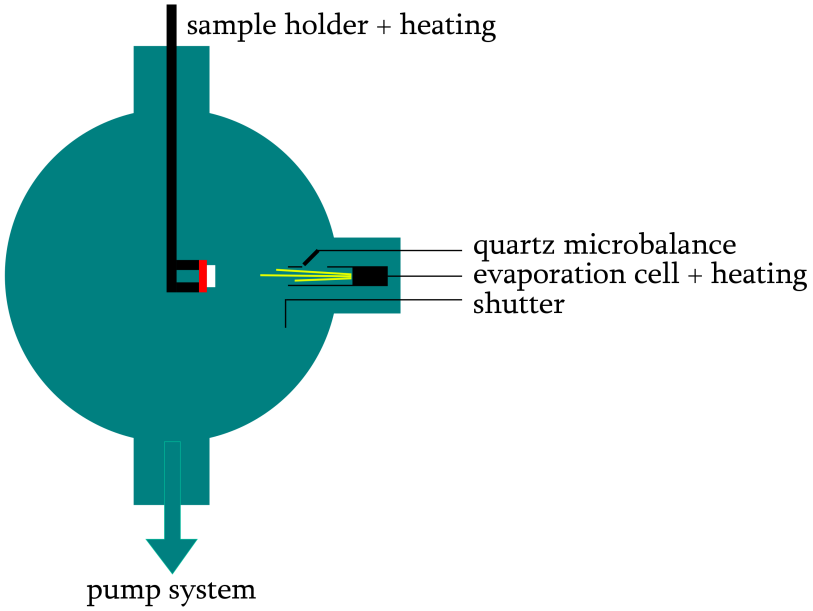

Figure 6: Sketch of the vacuum chamber used for the physical vapour deposition process

An electric current is used to heat up a wire (Joule heating) that is wound around the evaporation cell. In case of a metal cell the heating wire needed to be covered with an insulating material to prevent the cell from short-circuiting the heating cycle. When using an evaporation cell made of glass the heating wire has not been covered in an insulating material (see figure 7 right).
In case of a metal cell being used for evaporation the temperature of the source can be measured via a thermocouple that is attached to the back wall of the evaporation cell. This concept could not be applied to the glass cell and therefore, no source temperature measurement has been performed in that case.

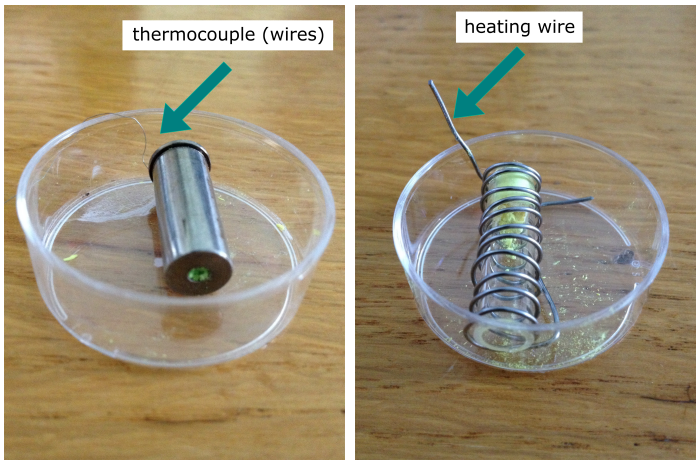

Figure 7: Pictures of the evaporation cells used for the physical vapour deposition process; left: metal cell (steel) with a hole diameter of ∼2.5 mm; (with thermocouple on the back); right: glass cell with an open end of ∼5 mm (with heating wire)

The sample holder is brought into the vacuum chamber from top. The sample was fixed to a plate facing horizontally by bending small metal pieces that are connected to the substrate holder over the edges of the substrate (with the help of tweezers). Due to the connection between the substrate and the sample holder being very loosely two metal springs have been used at both sides to ensure better mechanical contact and therefore, also better thermal contact between the substrate and the substrate holder (see figure 8). When put in, the whole sample holder (together with the substrate) can be turned so that the sample faces the hole of the evaporation cell directly. The plate where the sample is fixed to can be heated via Joule heating. The temperature of this plate (in best case also the temperature of the whole sample) is measured with the help of a thermocouple connected to the back of the plate (see figure 8).

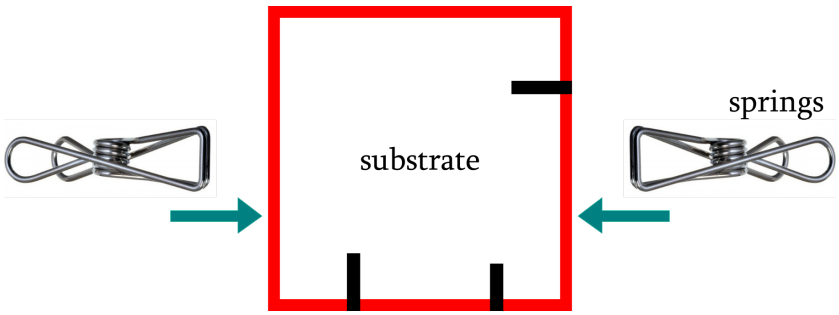

Figure 8: Sketch of the sample holder connected to the substrate via small metal pieces (black) - improvement of (thermal) contact by using metal springs

Despite the springs the thermal contact between the substrate holder and the substrate could be not homogeneous throughout the whole substrate due to inhomogeneities on the surface of the substrate holder. However, the springs improve the thermal contact as is shown in figure 9.

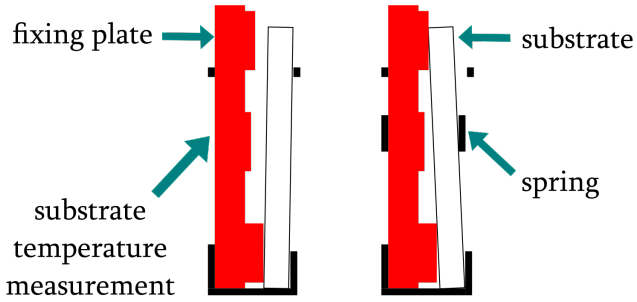

Figure 9: Sketch of the side view of the sample holder (exaggeratedly drawn inhomogenious surface) connected to the substrate via small metal pieces (black) - improvement of (thermal) contact by using metal springs

The three-stage pump system used in the evaporation chamber consists of a rotary vane pump as the first and two turbomolecular pumps as the second and third stages. This system can attain pressures as low as 10^{-8} mbar.

6.3 Evaporation cells

A metal Knudsen cell made of brass (thermal conductivity; see table 3) with a hole diameter of ∼0.7 mm was used and half filled with Alq(3) powder. A thermocouple at the back end of the cell made it possible to measure the temperature of the cell during evaporation. At a pressure of $\sim 6 \cdot 10^{-7}$ mbar the cell was heated up to 200°C.

Table 3: Thermal conductivity values (taken from [22]) of the materials that the evaporation cells used in the experiments are made of
λ . . . thermal conductivity

Material	λ / $\mathbf{Wm^{-1}K^{-1}}$
Brass	109
Steel	50.2
Glass	0.8

A quartz microbalance (see chapter 6.2) was used to monitor the amount of deposited/evaporated material. From former experiments on organic molecules in the deposition apparatus an educated guess for the factor converting the frequency shift on the QMB to a film thickness was made [23]:

$$c = 0.04 \text{ nm/Hz} \tag{6}$$

For a 50 nm film this corresponds to a frequency shift of 1250 Hz on the QMB. For a reasonable deposition time of 50 minutes the mean deposition rate would have to be 25 Hz/min or 1 nm/min.

In figure 10 the first heating cycle is plotted as deposition rate vs. temperature. The temperatures were set according to the direction of the arrowheads. While increasing the temperature of the source the frequency on the QMB starts to decrease slowly at ∼210°C which corresponds to starting evaporation/deposition. One can see a decrease in the deposition rate with increasing temperature above 255°C After cooling down to 255°C again the deposition rate was being let to stabilize for about 10 minutes to ∼1 Hzmin^{-1}. Reheating up to ∼300°C led to a small increase in the deposition rate. However, it did not surpass a value of ∼4 Hzmin^{-1}. This whole behaviour happened due to clogging of the hole of the Knudsen cell. Heating further than ∼300°C has not been performed because the melting temperature has been given by the manufacturer as >300°C (see table 2). After taking out the cell a

yellow fibrous grid could be seen clogging the hole of the cell. An XRPD spectrum similar to the spectrum given in figure 5 has been recorded for the material clogging the hole of the evaporation cell. The result is similar to that in figure 5 and therefore, the structure clogging the cell can be interpreted as crystals of the α-phase of Alq(3).

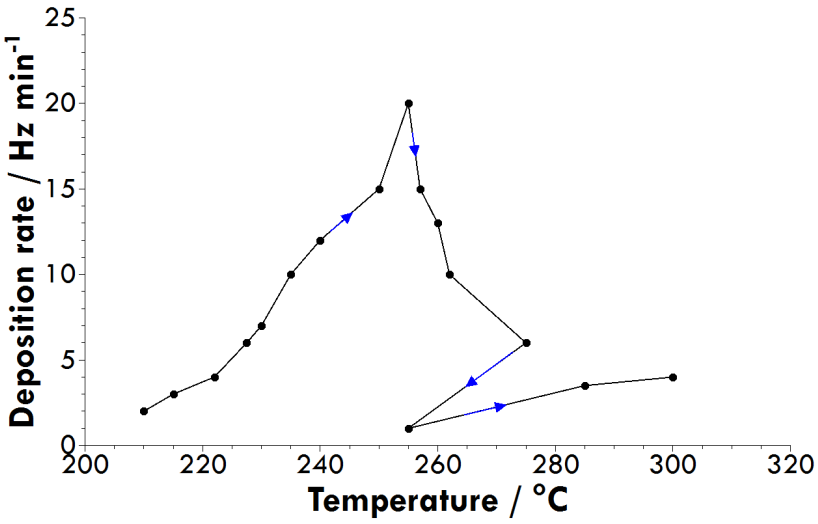

Figure 10: Deposition rate vs. temperature in the first heating cycle of the brass Knudsen cell (hole diameter ~0.7 mm)

After finishing the first heating cycle (see figure 10) the same evaporation cell was cleaned and refilled with less powder. The heating wire around the cell was redistributed so that it was very densely arranged at the front end of the cell (close to the hole) and the cell was carefully set in the profound position again (see figure 6.2).

The first heating cycle with the reset brass Knudsen cell is shown in figure 11. The temperature has been increased slower than in the case of the first time. At a temperature of 250°C the deposition rate dropped with increasing the temperature slightly/waiting for 15 minutes. This could again be associated to a clogging process. Again a yellow fibrous grid appeared to be grown across the hole of the cell.

As a consequence, a Knudsen cell (see figure 7 left) has been taken in which a hole with a diameter of ~2.5 mm has been drilled into. The cell was made of steel which manifests in the thermal conductivity being lower than the one of brass (see table 3). It has been filled and set into the vacuum chamber exactly like the brass Knudsen cell (as described above). At a similar pressure as the other cells were tried

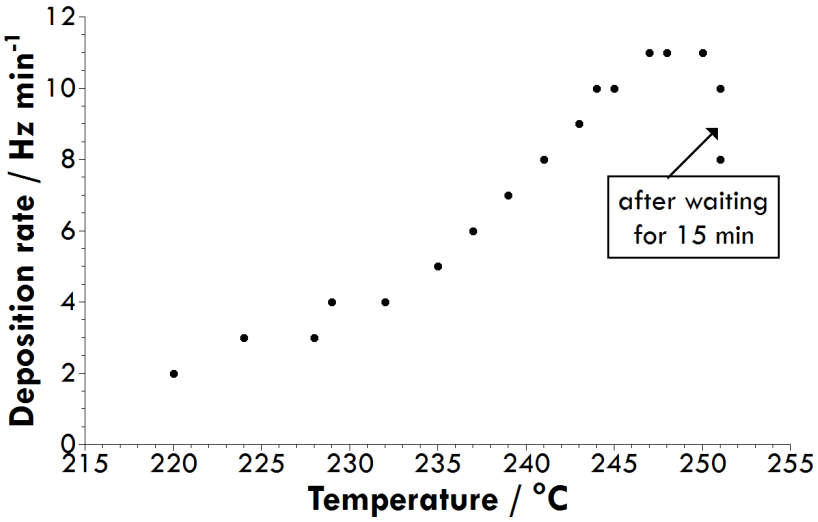

Figure 11: Deposition rate vs. temperature in the first heating cycle of the reset brass Knudsen cell (hole diameter ∼0.7 mm)

in the first heating cycle the deposition rate went up to ∼24 Hz/min by increasing the temperature up to 235°C. The full first heating process is shown in figure 12.

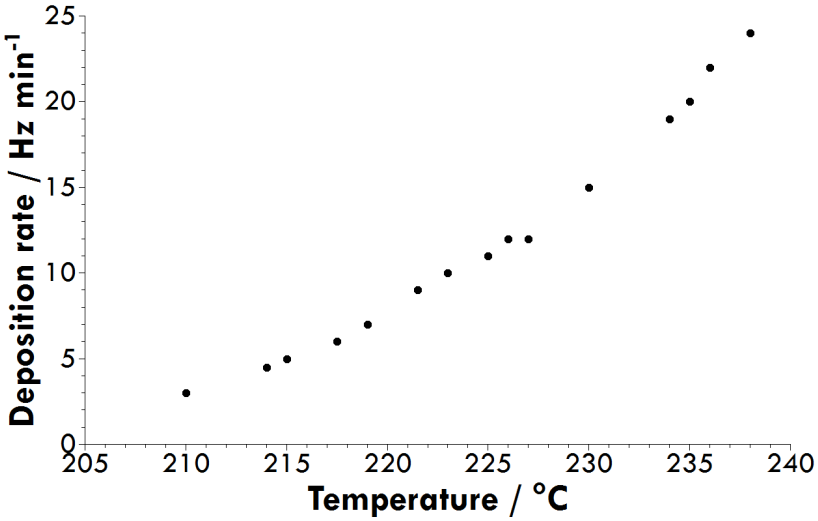

Figure 12: Deposition rate vs. temperature in the first heating process of the steel Knudsen cell with a wider hole (∼2.5 mm)

By reading off the heating current I and voltage U during an evaporation process of the steel evaporation cell the heating power $P = U \cdot I$ has been evaluated as a function of the source temperature T_{sub} (see figure 13).

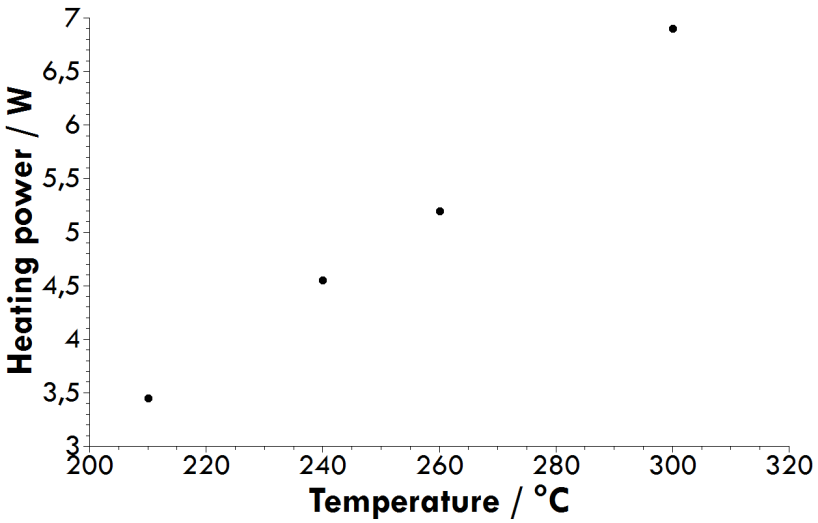

Figure 13: Heating power vs. source temperature for the steel Knudsen cell

As 25 Hz/min was the wanted deposition rate it was kept at this value for half an hour. It was stable for that period of time. A deposition process was started by opening the shutter. During the first hour of the deposition process the deposition rate dropped to ∼12 Hz/min which was thought to happen due to stabilization of the whole system (unwanted residues being evaporated and therefore, increasing the recorded deposition rate).

Heating the evaporation cell for a second time resulted in an immediate decrease of the deposition rate at 250°C from 20 Hz/min to 15 Hz/min. After a couple of minutes the deposition rate had dropped to about 5 Hz/min. After opening the chamber the 2.5 mm hole could be seen again covered with yellow fibres.

Finally, a 3 cm long glass cell has been used as the evaporation source (see figure 7 right). Glass has an even lower thermal conductivity than steel (see table 3). With an open end of ∼5 mm a new heating wire has been spun around the cell very tightly (without insulation). The cell has been filled to a third with Alq(3) powder (see table 2) and put into the evaporation chamber. A disadvantage of this set-up is that no thermocouple could be attached as in case of the metal cells and therefore, the temperature of the evaporation source could not be monitored. Also the current used to heat the cell could not be compared to that heating the metal cells due to the difference in length and diameter of the heating wires used. The source temperature as a function of the heating power ($P = U \cdot I$) was thought to be also different for the new set-up as the thermal conductivity (see table 3) of glass is different and also no electrical insulation has been used in the glass cell case. So just the signal of the QMB had to be used to monitor the evaporation process at a certain set current value. Due to that fact the first heating cycle had been performed very carefully because the point where evaporation would start could not be estimated before. The first heating process can be seen in figure 14. At every point the system could stabilize within 10 minutes.

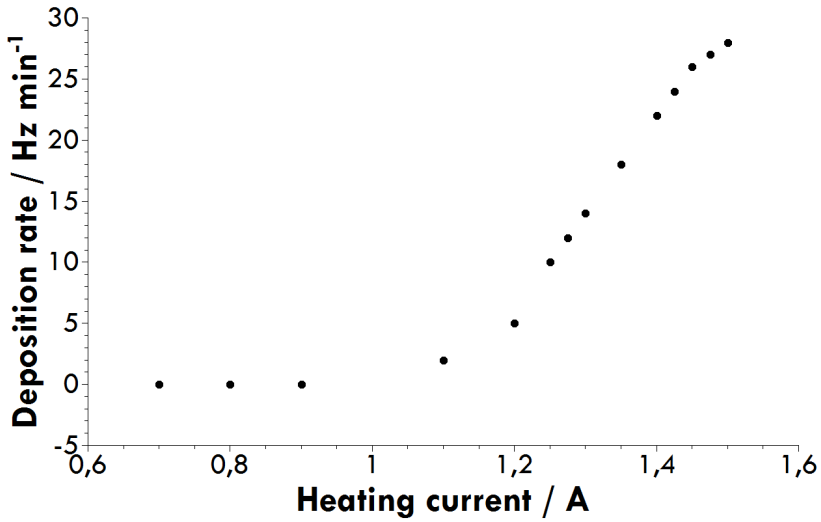

Figure 14: Deposition rate vs. temperature in the first heating process of the glass cell with an open end (∼5 mm)

After the first couple of heating cycles the evaporation cell gave stable/slightly decreasing but also slightly smaller deposition rates compared to the first cycle. Despite that fact the current can be readjusted so that the wanted deposition rate is achieved and kept stable for an entire deposition process. The heating power has been evaluated to be in a similar range for all the deposition processes performed with the glass cell compared to the heating power evaluated for the metal cell (see figure 13). Although the thermal conductivity of glass is different and no electrical insulation had been used around the heating wire in the glass cell case these similar heating power values would correspond to source temperatures of about 250°C.

The powder from the source has been investigated after several deposition processes by XRPD. From the XRPD data no change in comparison to the spectrum of the as received powder (see figure 5) could be found.

6.4 Substrates

Silicon wafers with a layer of thermal oxide (SiOx) on top from *Siegert Wafer* have been used as substrates. The low surface roughness and good availability have been crucial factors for the usage. The following properties are given by the manufacturer (see table 4):

Table 4: Properties of the Si wafers used as substrates (as given by the manufacturer)

Property	**Value**
Manufacturer	Siegert Wafer GmbH
Size	10 x 10 mm^2 ($\pm$0,1 mm)
Thickness	(675 $\pm$ 25) μm
Thermal oxide	150 nm $\pm$ 5% (dry)
Orientation	<100>

6.5 Substrate cleaning

The substrates described in section 6.4 were cleaned before putting them into the evaporation chamber. The following cleaning procedure has been used for all the substrates:

1. Rinsing beaker and substrate holder with acetone
2. Wiping substrates with tissue paper moistened in acetone
3. Ultrasound bath in acetone for 15 minutes
4. Rinsing beaker and substrate holder with isopropanol
5. Wiping substrates with tissue paper moistened in isopropanol
6. Ultrasound bath in isopropanol for 15 minutes
7. Cleaning with CO_2-spray

XRR measurements have been performed to compare the substrates before and after this cleaning procedure. The results of this comparison can be found in section 6.6.

6.6 Investigation of the substrate surface

To get a comparison of the cleanliness of the substrate surface before and after cleaning X-ray reflectivity measurements have been performed on the cleaned and uncleaned substrates with the diffractometer described in section 7.2. The measured data has been fitted with the software *X'Pert Reflectivity*. As an input the software needs to be given a layered structure with borders for thickness, roughness and density values. Despite the cleaning it was not possible to get results from the fit that show good compliance with the measured data without adding an unknown debris layer. The results of the fit together with the measured data for the cleaned substrate can be found in figure 15.

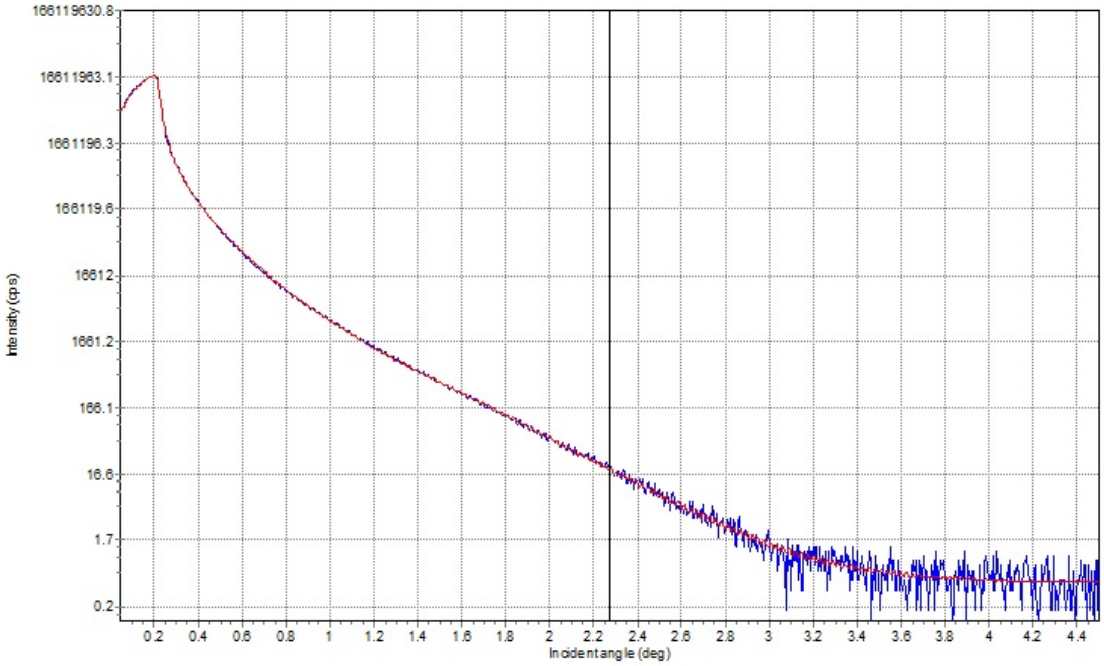

Figure 15: Result of the X-ray reflectivity measurement of a cleaned substrate (blue); fit with *X'Pert Reflectivity* (red)

The parameters obtained from the fit with *X'Pert Reflectivity* for the cleaned substrate can be found in table 5.

An XRR measurement curve with the same settings as for the cleaned substrate was recorded for an uncleaned Si/SiOx-substrate (see figure 16). Again a fit with *X'Pert Reflectivity* has been performed. The results are shown in table 6.

Table 5: Parameters obtained from the fit of the measured X-ray reflectivity data from a cleaned substrate
d . . . layer thickness
ρ . . . density of the material
σ . . . surface / interface roughness

Layer	**d / nm**	ρ **/ g cm^{-3}**	σ **/ nm**
Debris	0.01	1.1	0.5
SiOx	157.7	2.17	1.37
Si (Substrate)	–	2.23	0.02

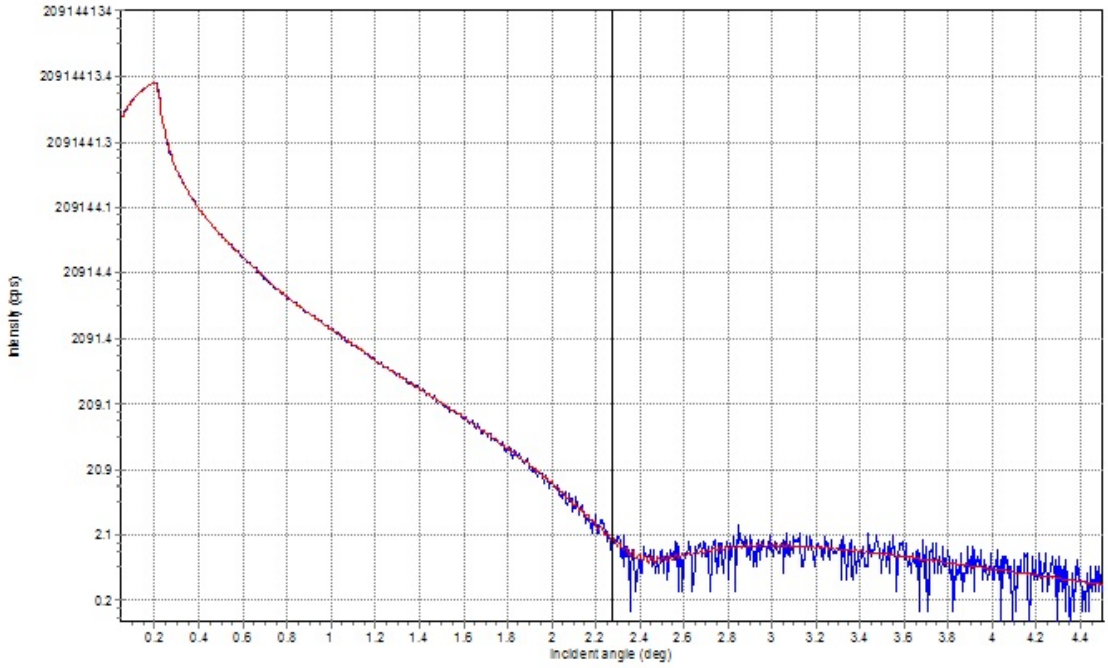

Figure 16: Result of the X-ray reflectivity measurement of an uncleaned substrate (blue); fit with *X'Pert Reflectivity* (red)

Table 6: Parameters obtained from the fit of the measured X-ray reflectivity data from an uncleaned substrate
d . . . layer thickness
ρ . . . density of the material
σ . . . surface / interface roughness

Layer	**d / nm**	ρ **/ g cm^{-3}**	σ **/ nm**
Debris	0.9	1.1	0.6
SiOx	157.3	2.16	1.25
Si (Substrate)	–	2.20	0.3

The fitted data of the cleaned and uncleaned substrates (listed in tables 5 and 6) show good compliance with the measured curves. From this it is clearly visible that the cleaning procedure fulfils its purpose as the debris layer could be reduced from 1 nm without cleaning to basically none after the cleaning procedure has been applied. However, without adding the unknown debris layer in the fit software the data could not be fitted. This suggests that there are still some residues (probably organic) left after cleaning even though they seem to be very small/few.

6.7 Preparation of Alq(3) thin films

The heating power was set to achieve the right cell temperature conditions (via the current through the heating wire) to get stable evaporation from the glass cell. The cleaned substrates were placed on the substrate holder as described in section 6.2. Vacuum conditions were achieved using the pump system described in section 6.2. All the coating processes have been performed at pressures in the range of 10^{-6} - 10^{-7} mbar.

A series of first samples prepared with the PVD chamber using the glass evaporation cell (see chapters 6.2 and 6.3) has been investigated by XRR to get a conversion factor that connects the frequency shift on the quartz microbalance to the thickness of the deposited film. The software *X'Pert Reflectivity* provides two methods to obtain the film thickness from the recorded data:

- The direct method calculates the film thickness from the critical angle of total reflection of the material at hand and the first and second Kiessig fringe angles.
- The Fourier method also needs the critical angle of total reflection but "finds" the Kiessig fringe angles from being given a start and an end angle in the measured curve. This gives a plot of the Fourier magnitude over the thickness with peaks at certain thickness values obtained from periodic fringe structures in the data.

The following table (table 7) shows a list of samples (deposition from glass cell) together with the frequency shift on the quartz microbalance with the mean thickness value obtained from the *X'Pert Reflectivity* program with the two described methods.

From the data in table 7 one can see that the conversion factor for sample number 4 would be totally different to the other samples. This can be attributed to sample number 4 being used as the first substrate for a deposition process from the glass cell. The whole vacuum system needs time to stabilize and also the glass cell will emit unwanted species during the first couple of heating cycles. The data from all the other samples shows more reproducibility but due to the substrate temperatures being not the same for all the samples the structures appearing on the films are different and therefore XRR as an integral technique has its limitations due to the inhomogeneity of the thin films. Nevertheless, the mean conversion factor for the frequency shift on the quartz microbalance to a thickness value could be derived

Table 7: List of samples with the frequency shift on the quartz microbalance (Δf) and the thickness value obtained by X-ray reflectivity (d)
N° ... sample number
c ... conversion factor (frequency shift to thickness)

N°	**d / nm**	**Δf / Hz**	**c / nmHz^{-1}**
4	125	2500	0.05
6	145	2100	0.069
7	117	1650	0.071
8	125	1700	0.074
9	138	1900	0.073
10	130	1900	0.068
16	50	750	0.067

with standard deviation from the data shown in table 7 (without data of sample 4):

$$c_{mean} = (0.070 \pm 0.003)\ \text{nm/Hz} \tag{7}$$

This can be compared to the conversion factor used to decide about the wanted deposition rate (see equation 6). The difference is caused by the different molecules used and translates to a deposition time of about 1 hour for Alq(3) thin films of a nominal thickness of 100 nm.

Table 8: List of samples prepared at substrate temperatures T_{sub}
N° ... sample number
* ... no film on substrate after deposition process

N°	**T_{subs} / °C**
4	25
6	50
7	75
32	100
9	140
24	150
17	160
26	165
27	170
28	172
30	173
29	174*
25	175*

The conversion factor given in (7) has been used for all further deposition processes and the nominal thickness values are given from now on if not mentioned explicitly otherwise. A list of samples with a nominal thickness of 100 nm prepared at several different substrate temperatures can be found in table 8. As a mean deposition rate ∼1.4 nm/min has been set via the conversion factor given in (7).
A study about the influence of the deposition rate on the morphology of Alq(3) thin films and the performance of luminescent devices has been performed by Cheng et al. [24]. Device performance is the reason that several groups [25] [26] use higher deposition rates. However, several references also use similar deposition rates to the ones used in this work [27] [28].

As noted in the list of samples prepared at several different substrate temperatures given in table 8 the samples prepared at substrate temperatures above 173°C do not contain any film deposited on the substrates after a completed evaporation procedure. This happens due to the temperature being in a range where desorption of Alq(3) molecules dominates the process of molecules impinging on the substrate and sticking to it. As Brinkmann et al. [3] report that this is the case for temperatures above ∼167°C using passivated Si(100) wafers or quartz slides as substrates and Jian et al. [26] still get Alq(3) films at substrate temperatures as high as 180°C on indium tin oxide (ITO) substrates or sapphire plates this onset temperature seems to vary. In the works of Brinkmann et al. [3] and Jian et al. [26] studies about the surface roughness behaviour of Alq(3) films deposited by PVD varying the substrate temperature can be found. Lots of factors not only influence the desorption temperature but also this surface roughness behaviour with respect to the substrate temperature during deposition. Some of these could be differences in the substrates used or differences in the deposition procedure itself (from vacuum conditions to thermal contacts to deposition rates).

In the following sections the samples given in table 8 are investigated with respect to their morphology, surface appearance and crystallinity. All in all, the aim is the phase analysis of the structures occurring on the different samples.

7 Experimental section - sample investigation

In the following sections the techniques to investigate the samples prepared by the methods described in section 6 are elaborated.

7.1 Optical microscopy

Images using optical microscopy in reflection have been taken with an optical microscope from *Olympus* described in table 9.

Table 9: Properties of the optical microscope of the institute used to investigate the thin films

Property	Description
Model	BX51 from Olympus (Tokio, Japan)
Digital camera	Olympus Camedia C-5060 WideZoom
Software	Olympus DP-Soft 5.0
Ocular	WH10x/22
Object lenses	UMPlanFI (magnification/numerical aperture)
	5x/0.15, 20x/0.46, 50x/0.80, 100x/0.95

Figures 17-20 show optical microscopy pictures of samples prepared at different substrate temperatures. Films prepared at substrate temperatures below 100°C do not show any structures that result in contrast visible in the optical microscope. However, one can see inhomogeneities on samples prepared at substrate temperatures above 100°C. Optical microscopy makes it possible to distinguish smaller structures on these samples. As described in section 6.2 the inhomogeneous thermal contact between the heated substrate holder and the substrate could result in

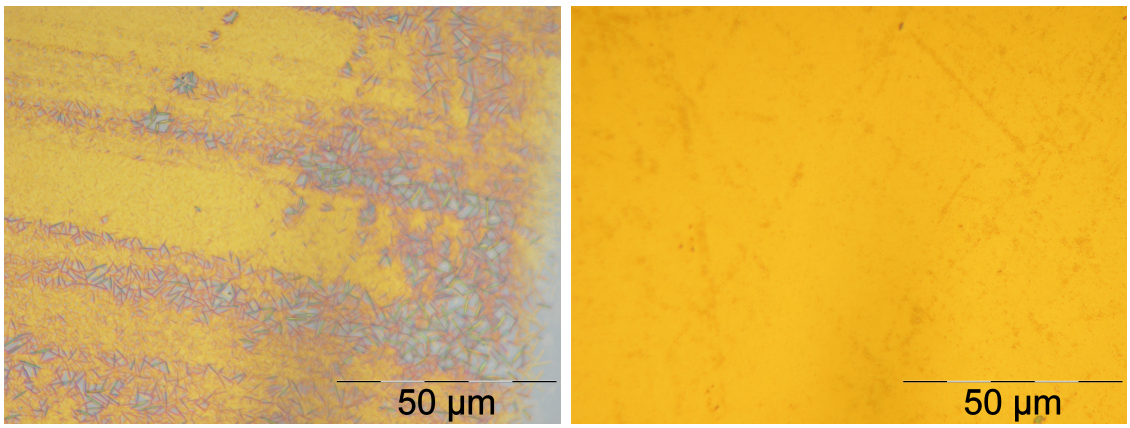

Figure 17: Microscopy pictures of a sample prepared at a substrate temperature of T_{sub} = 100°C; left: close to edge of sample; right: middle of sample

inhomogeneous growth behaviour of Alq(3) structures on the substrate. Pictures of structures on the edges or close to substrate holders (presumably higher temperatures) compared to pictures of structures in the middle of the films are shown in the mentioned figures (17-20).

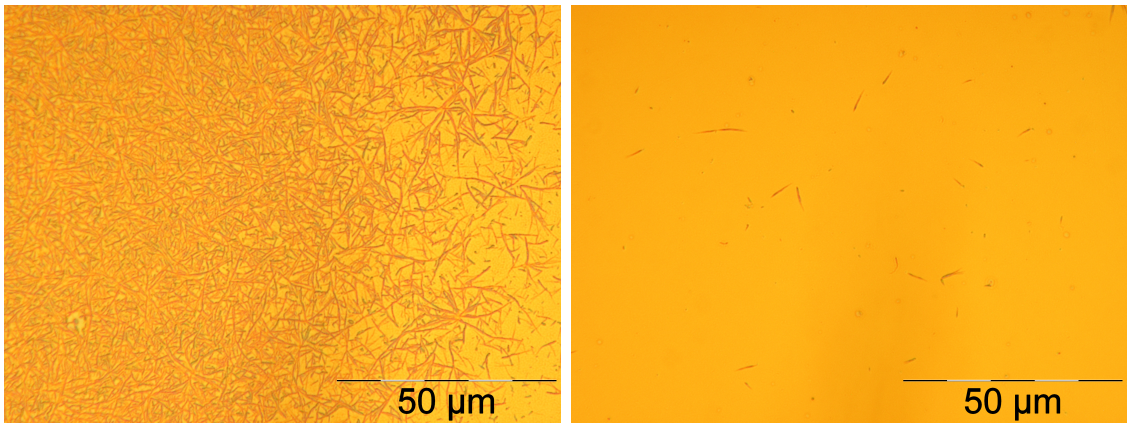

Figure 18: Microscopy pictures of a sample prepared at a substrate temperature of T_{sub} = 150°C; left: close to edge of sample; right: middle of sample

The structures causing contrast in the microscopy pictures shown in figure 18 are of needle-like shape. This is in accordance with the fact that α-phase Alq(3)-crystallites exhibit needle-like morphology [3]. The picture on the left shows inhomogeneously dense and inhomogeneously long needles occurring at an area of the sample that has been close to metal springs connecting the substrate to the heated substrate holder during deposition. Also in a region considered to exhibit lower temperatures due to bad thermal contact between the substrate holder and the substrate in the middle of the sample needle-like structures appear. However, nucleation seems to be restricted to very few spots in this area compared to regions close to the metal springs as described before. The needle-like structures appear to grow in length until they grow together (see figure 18) as there are more long needles (length of 10 μm) in regions where there are less in total number. In regions of densely arranged needles the longer ones seem to be connected by a grid of shorter (2-5 μm) needle-like structures.

Figure 19 shows microscopy pictures of different regions on a sample prepared at a substrate temperature of 172°C. In the middle of the sample (right picture) the few needles are accompanied by a dotted structure in between them. Close to the edge of the sample (left picture) the majority of needles exhibit a length of

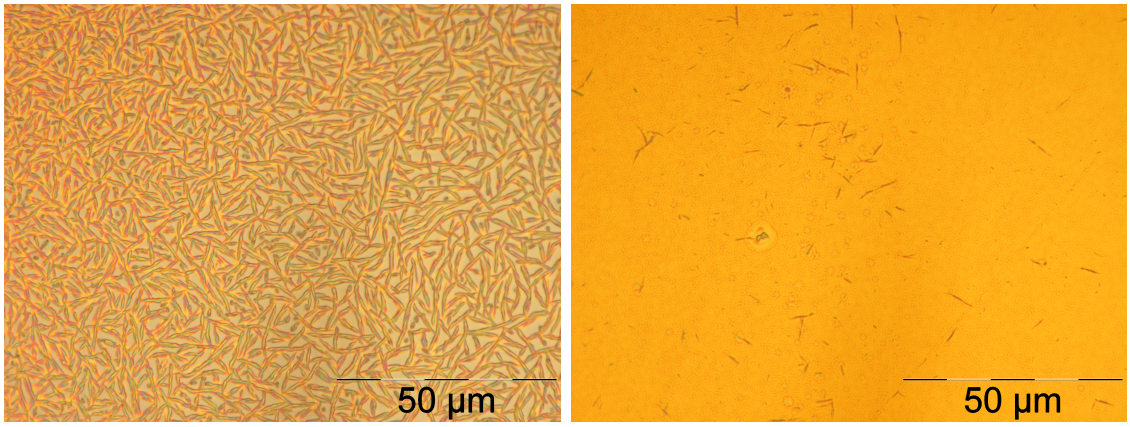

Figure 19: Microscopy pictures of a sample prepared at a substrate temperature of T_{sub} = 172°C; left: close to edge of sample; right: middle of sample

7-10 μm. With a few short needles (2-4 μm) in between those long needles the area in between these structures seem to be very flat resulting in low contrast. This could be explained by needles directly lying on the silicon oxide substrate surface without an Alq(3) film or needles covering it. Compared to the needles occurring on the film prepared at a substrate temperature of 150°C (see figure 18) the needles exhibit a larger width which results in the needles also showing thickness interference and causing colour contrast within a single needle.

The microscopy pictures in figure 20 show that needle-like structures occur at both regions investigated on the sample prepared at 172°C substrate temperature. In the picture on the left even thicker needles (1-2 μm) compared to the picture in figure 19 (left) are visible. Furthermore, this picture exhibits colour contrast all

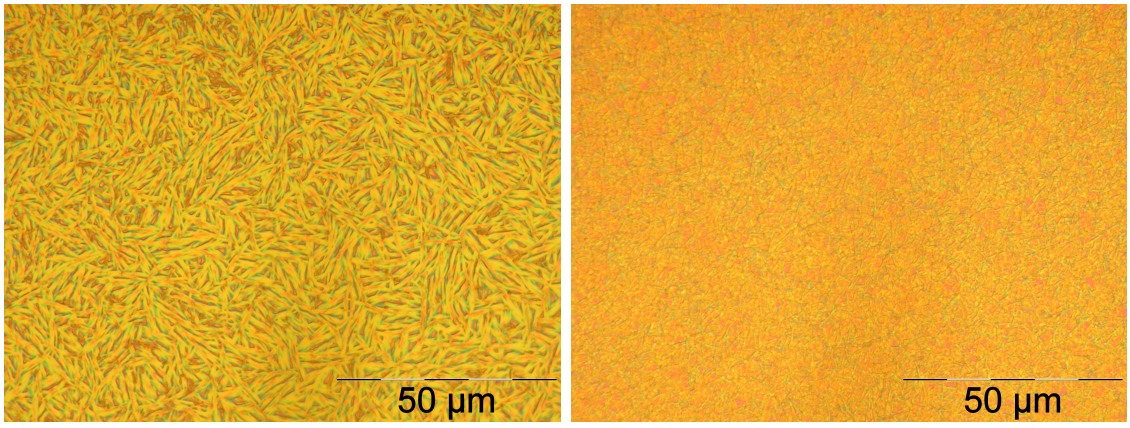

Figure 20: Microscopy pictures of a sample prepared at a substrate temperature of T_{sub} = 173°C; left: close to edge of sample; right: middle of sample

over the investigated area (also in between the needles) and therefore a dense grid of needles appears. Most of the needles seem to be in the range of or longer than 10 μm with just very few being shorter than 5 μm. In the middle of the sample (right picture) many long (5-10 μm) needles occur in between a grid of small structures being not possible to investigate further with the help of optical microscopy.

Comparison of the pictures shown in figures 17-20 leads to the conclusion that the structures causing contrast in the optical microscope increase in number and in size with increasing substrate temperature.

7.2 PANalytical Empyrean

All X-ray reflectivity (XRR) and specular X-ray diffraction (XRD) measurements have been recorded on the diffractometer of the institute - the *PANalytical Empyrean*. An overview of the diffractometer is given in figure 21. It is a measurement device where the X-ray tube, the sample stage and the detector unit can be moved. This allows for investigation of the whole orientation space. The X-ray tube is powered with 40 mA at 40 kV and uses a copper anode. Beam masks of 4 mm in width and divergence slits of 1/32° for XRR and 1/8° for XRD have been used. A parallel beam mirror acts as a collimator and also a monochromator to emit mainly Cu K_α radiation. A programmable beam attenuator is used as a protection against very high intensities that could possibly destroy the detector. This is done by positioning a 0.125 mm thick Ni plate in the beam in case of the intensity surpassing a pre-set count value. A 0.02 rad Soller slit and an anti-scatter slit of 0.1 mm for XRR and 7.5 mm for XRD have been used. The diffractometer utilises a *PIXcel*^{3D} solid state detector with a pixel matrix of 255x255 and pixel sizes of 55x55 μm. The detector is used in receiving slit mode (as a point detector) for the XRR measurements and in the scanning line mode for XRD measurements where the sum of each pixel line gives the intensity for a specific 2Θ value.

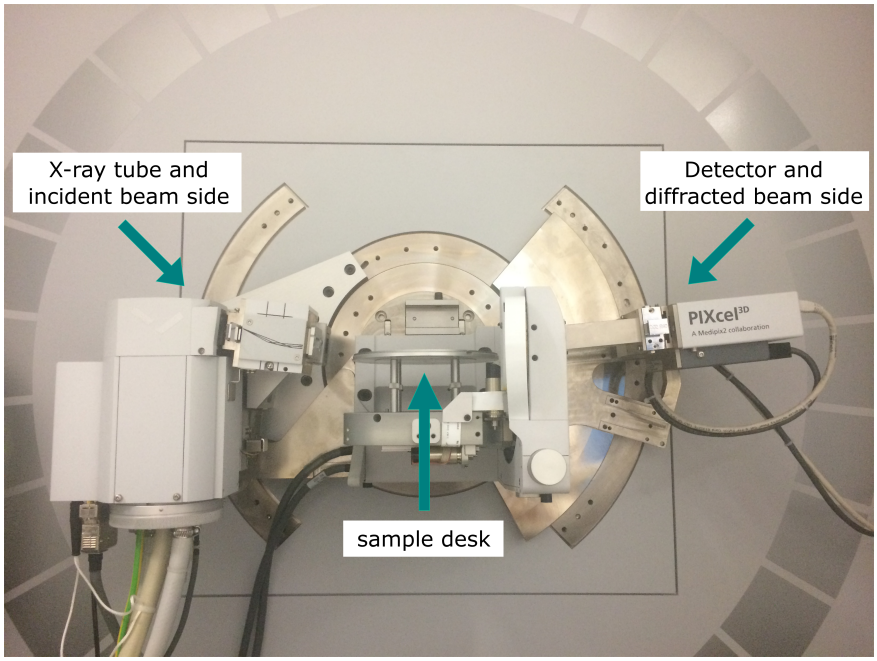

Figure 21: Photo of the diffractometer used for all X-ray reflectivity and specular X-ray diffraction measurements

7.3 X-ray reflectivity (XRR)

All XRR measurements have been performed with the diffractometer described in section 7.2. A non-reflecting Si block has been used between the sample desk and the sample.

A series of samples prepared at different substrate temperatures during deposition with a nominal thickness of 100 nm has been investigated by means of XRR between 2Θ values of 0.01° and 9°. The measurement curves are shown in figure 22 up to 2Θ values of 5° because of the noise of all measurement curves interfering in a way that no clear trend can be seen at angles (2Θ) higher than 5°.

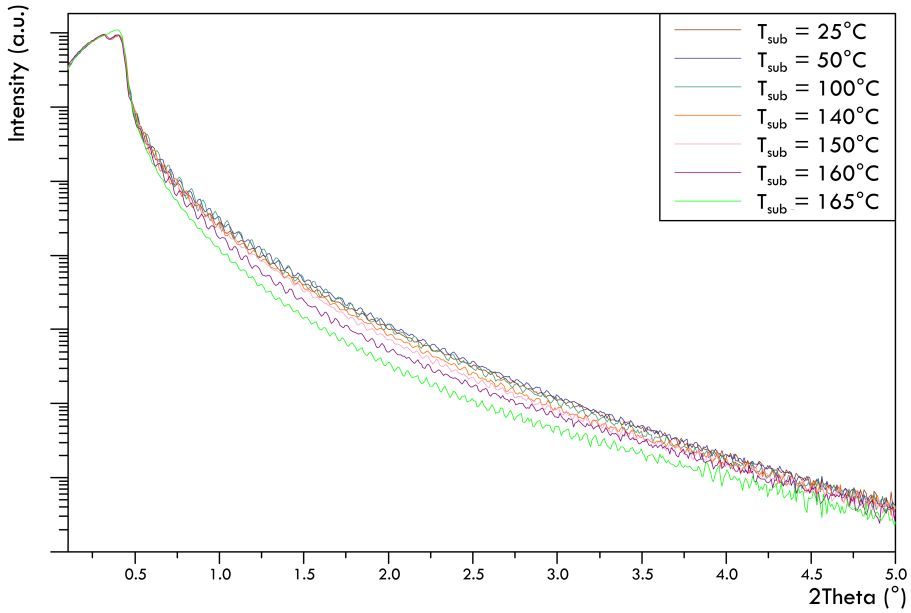

Figure 22: Results of X-ray reflectivity measurements on a series of samples prepared at several different substrate temperatures ranging from 25°C to 165°C (see T_{sub} in the legend)

The series of XRR measurements of samples prepared at different substrate temperatures (see figure 22) shows good compliance of the critical angles of the substrate and the Alq(3) layer of the different samples (see figure 23). However, the signal recorded for the sample prepared at a substrate temperature of 165°C shows just one distinct critical angle of total reflection. The values have been read out of the measurement curves with the help of the *DataViewer* software at the half of the maximum intensity after the two respective maxima occurring in the plotted curves

in figure 22. The angle α_{c1} can be attributed to the critical angle of total reflection of the Alq(3) thin film whereas α_{c2} respectively corresponds to the critical angle of total reflection of the silicon substrate and is also close to the theoretical value for a wavelength of the Cu K_α line of 1.5418 Å of $\alpha_{cSi} = 0.224°$ [29]. The compliance of the critical angles for all the measurements shows that the alignment has been successful and stable and that the density of the material in the films does not change significantly with varying the substrate temperature. The mean values with standard deviation for the critical angles (see figure 23) of Alq(3) and SiO_2 have been experimentally evaluated to

$$\alpha_{cAlq(3)} = (0.17 \pm 0.01)°$$
$$\alpha_{cSiO_2} = (0.22 \pm 0.01)°.$$

These angles can be used to evaluate the electron density ρ_e of both materials with equation 2.

$$\rho_{eAlq(3)} = (4.1 \pm 0.5) \cdot 10^{29}\ \mathrm{e^-/m^3}$$
$$\rho_{eSiO_2} = (6.9 \pm 0.6) \cdot 10^{29}\ \mathrm{e^-/m^3}$$

By knowing the molar masses M (see section 6.1) and [30]) and the number of electrons of one molecule N_e (Alq(3) - 238 e^-; SiO_2 - 30 e^-) the mass density ρ can be determined with the help of the Avogadro constant N_A (see equation 8).

$$\rho = \frac{\rho_e}{N_e} \cdot \frac{M}{N_A} \tag{8}$$

$$\rho_{Alq(3)} = (1.3 \pm 0.2)\ \mathrm{g/cm^3}$$
$$\rho_{SiO_2} = (2.3 \pm 0.2)\ \mathrm{g/cm^3}$$

The value of the mass density of the amorphous silicon oxide lies in a plausible range [30]. By knowing mass densities of other solid organic compounds [31] this can also be stated for the mass density value of Alq(3).

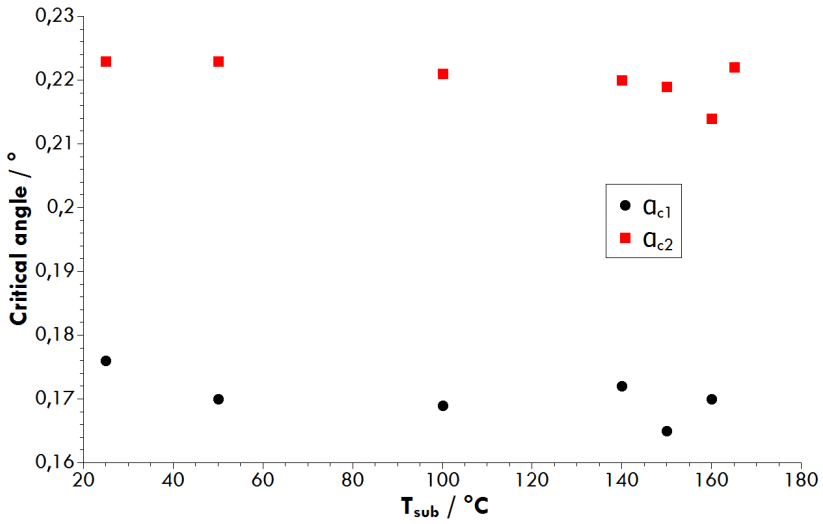

Figure 23: Critical angles (α_{ci}) of the samples of which the X-ray reflectivity data is shown in figures 22 and 26 for various substrate temperatures during deposition (T_{sub})

The decreasing slope of the measurement curves in figure 22 at angles slightly above the critical angle of total reflection with increasing temperature (see equation 1) allows to estimate that the surface roughness increases with increasing substrate temperature.
Equation 1 makes it also possible to plot the logarithm of the intensity I multiplied by the scattering vector q (see equation 5) to the power of four (see figure 24) versus q^2. As a result, the slope of the measurement curve at scattering vectors $q > 3q_c$ gives the surface roughness σ_{rms}. Using both critical angles the slopes have been fitted in figure 24 starting from the respective values.

From figure 24 the surface roughness σ_{rms} could be determined from the fitted slopes at scattering vectors with $q > 3q_c$ for all the samples listed in the legend of figure 24. The results are shown in table 10.

As it is known from other techniques (AFM - see section 7.4) that the surface roughness values should be much higher for the Alq(3) samples prepared at elevated substrate temperatures obviously the technique comes to its limits when subject to higher surface roughness as described in section 5.2.1. Despite that fact the roughness value for the blank substrate is in a plausible range. Also the sample prepared at a substrate temperature of 50°C appears to have a roughness in the given range as

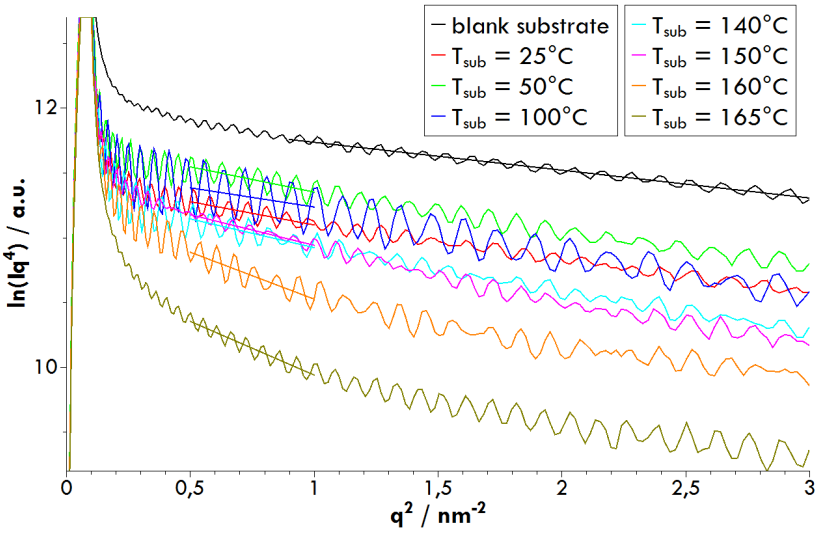

Figure 24: $\ln(Iq^4)$ vs. q^2 for Alq(3)-films prepared at several substrate temperatures and a blank substrate; the fitted slopes are shown as lines in the respective colour for all measurement curves

Table 10: List of roughness values for the different samples evaluated from the slopes in figure 24
T_{sub} ... substrate temperature during deposition
σ_{rms} ... surface roughness (route mean squared)

Sample	σ_{rms} / **nm**
blank substrate	0.45
T_{sub} = 25°C	0.6
T_{sub} = 50°C	0.62
T_{sub} = 100°C	0.55
T_{sub} = 140°C	0.66
T_{sub} = 150°C	0.69
T_{sub} = 160°C	0.84
T_{sub} = 165°C	0.9

is verified by the AFM measurements (see section 7.4). The method gives reliable results for the surface roughness at small scattering vectors and for the interface roughness as the scattering vector increases and the X-rays penetrate further into the different layers. This causes the measurement of a convolution of the surface roughness and the interface roughness at the same time. Layered structures are therefore a problem for this technique and thus give surface roughness values for the Alq(3) samples that do not represent the correct roughness values for the Alq(3) layer.

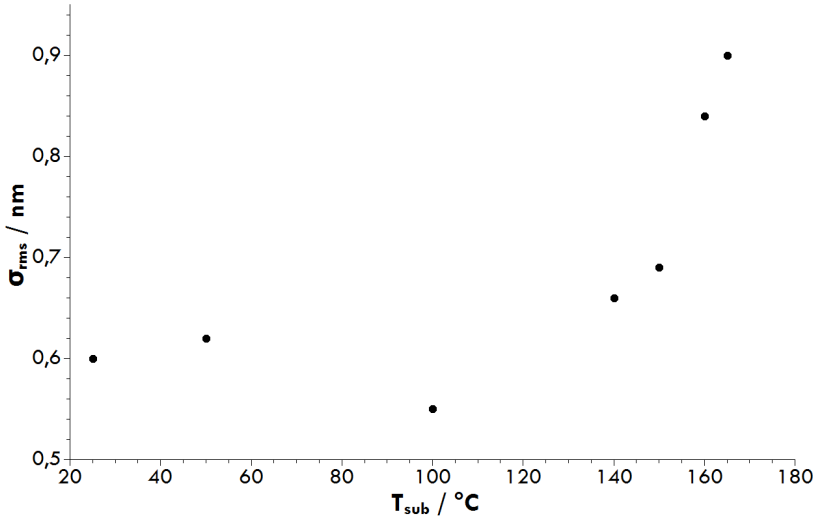

Figure 25: Surface roughness σ_{rms} vs. substrate temperature during deposition T_{sub} gained from the X-ray reflectivity measurements

Despite that fact the surface roughness behaviour with increasing substrate temperature during deposition shows a clear increasing trend throughout the range of investigated substrate temperatures. The data about the surface roughness behaviour with increasing substrate temperature during deposition (see table 10) has been plotted and can be found in figure 25 (compare to section 7.4). However, a decrease of the surface roughness between 50°C and 100°C substrate temperature can be recorded by XRR. A similar trend has been reported by Jian et al. [26] where the decrease in surface roughness in a substrate temperature range of 90°C and 120°C has been explained by a transformation from the low temperature meridional isomer of Alq(3) to the high temperature facial isomer of Alq(3) in that temperature range. Other groups report different surface roughness behaviours [25], [27], [32]. As stated before many factors can influence this trend.

An XRR measurement curve recorded on a sample prepared at a substrate temperature of 165°C is shown in figure 26 in a range of 2Θ values between 0.01° and 9°. As described above the XRR signal plotted in figure 26 shows only one distinct critical angle of total reflection close to the theoretical value of silicon oxide. That can be attributed to the XRR technique coming to its limits concerning surface roughness (as described in section 5.2.1). However, the curves obtained from XRR measure-

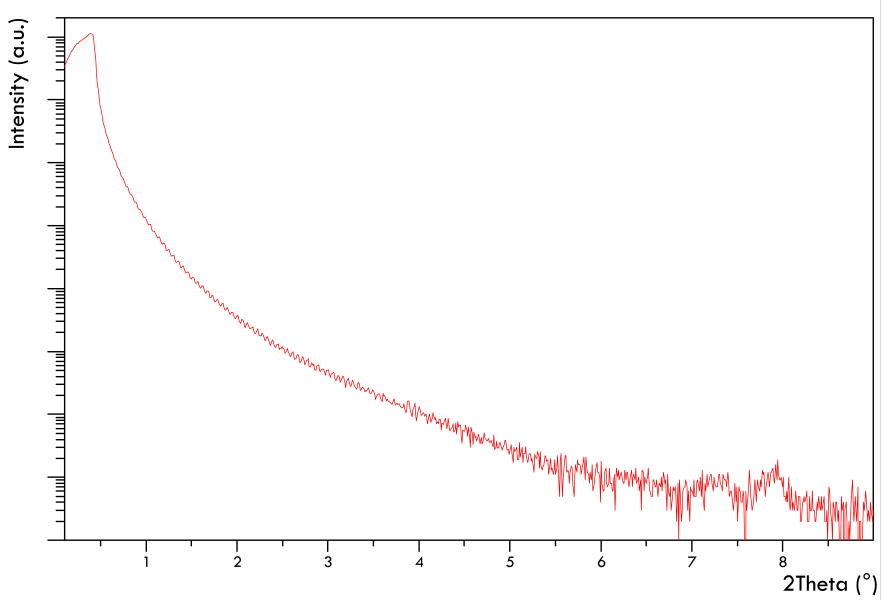

Figure 26: Result of an X-ray reflectivity measurement on a sample prepared at a substrate temperature of 165°C

ments on samples prepared at substrate temperatures above 160°C (so also the signal in figure 26) show the on-set of two Bragg peaks at angles of $2\Theta_1 = 7.35°$ and $2\Theta_2 = 7.95°$. With the used wavelength of $\lambda = 1.5418$ Å the lattice spacings of $d_1 = 1.2$ nm and $d_2 = 1.1$ nm respectively could be determined with the help of Bragg's law (see equation 3). This corresponds to lengths of the scattering vector of $q_1 = 0.52$ Å^{-1} and $q_2 = 0.56$ Å^{-1}. This leads to the conclusion that the samples prepared at substrate temperatures in that temperature range exhibit crystalline structures.

For further investigation of the crystallinity of the samples the methods of specular X-ray diffraction, grazing incidence X-ray diffraction and lattice phonon Raman spectroscopy have been applied. The results of these techniques can be found in sections 7.5, 7.6 and 7.7 respectively.

7.4 Atomic force microscopy (AFM)

Atomic force microscopy investigations have been performed with a *Nansurf Easyscan 2 AFM* on a vibration isolation table (*TableStable TS-150*). A *Schaefer-Tec POINTPROBE-PLUS* tip made of n^+-silicon has been used. The scanning area has been set to 5x5 μm^2. The software package *Gwyddion* has been used to plot and evaluate the AFM measurements.
3D images of the topography of the surface of a list of samples prepared at substrate temperatures between 25°C and 172°C are shown in figures 27-30.

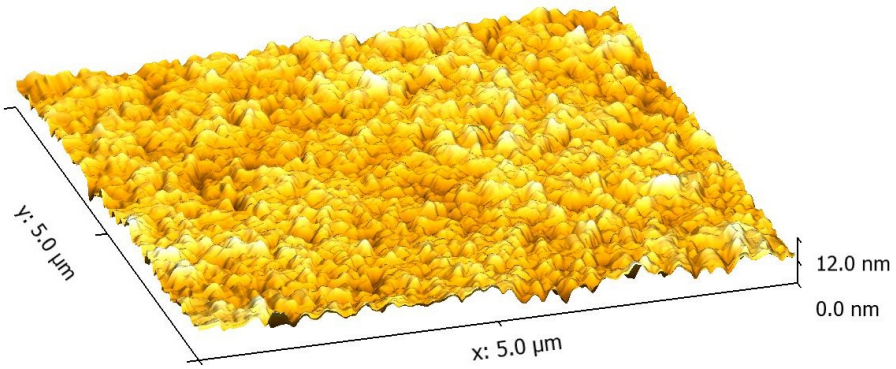

Figure 27: Result of the atomic force microscopy measurement of a sample prepared at a substrate temperature of 25°C

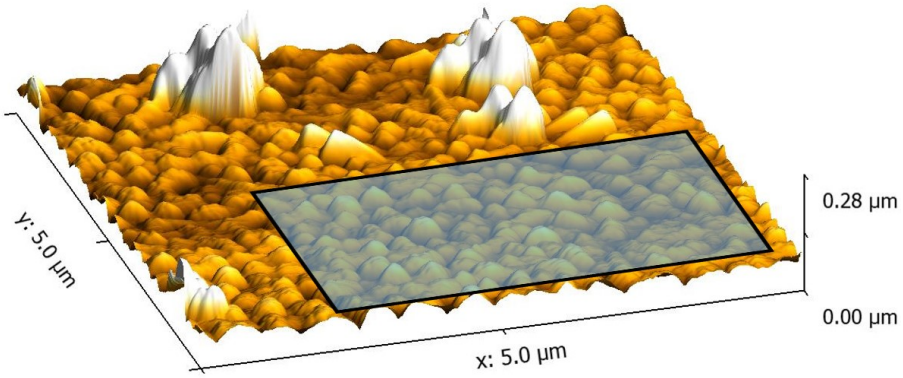

Figure 28: Result of the atomic force microscopy measurement of a sample prepared at a substrate temperature of 100°C; the surface roughness has been evaluated in the depicted area (black contour)

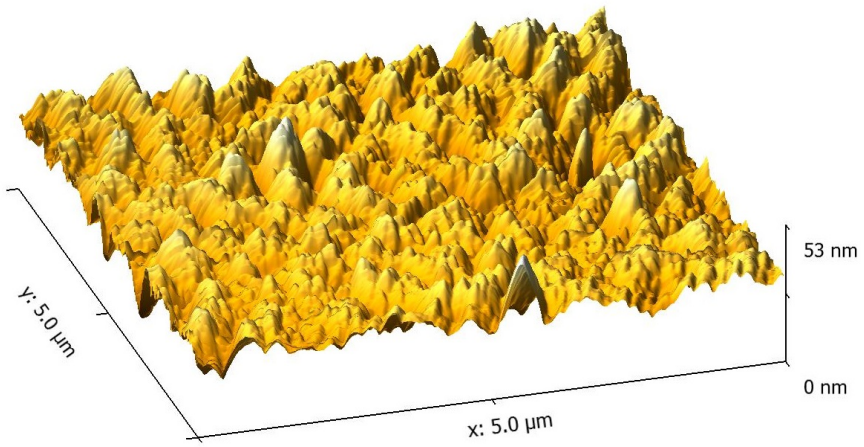

Figure 29: Result of the atomic force microscopy measurement of a sample prepared at a substrate temperature of 150°C

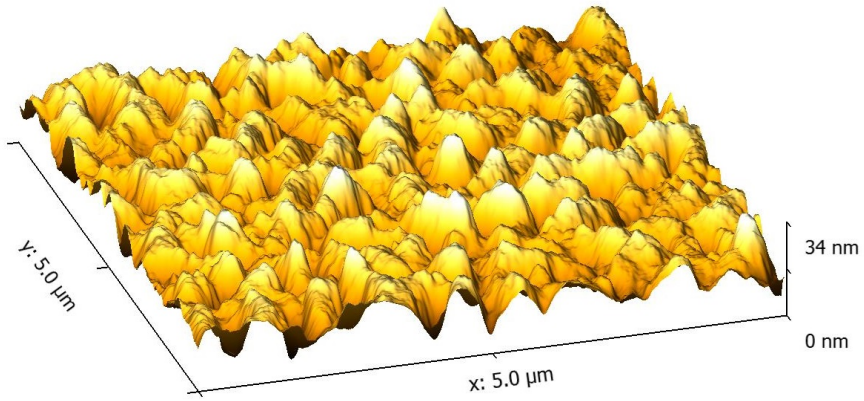

Figure 30: Result of the atomic force microscopy measurement in the middle of a sample prepared at a substrate temperature of 172°C

From the AFM measurements shown in figures 27-31 the surface roughness σ_{rms}, the maximum height registered and the average height of the surface could be evaluated via *Gwyddion*. The results can be found in table 11.

The maximum and average height of the surface (see table 11) are given by the difference between the lowest and highest measured point by the AFM tip on the surface and by an average of all height values over the surface covered by the AFM measurement. The data in table 11 shows that the surface roughness exhibits an increasing trend with increasing substrate temperature during deposition. Also the maximum height difference on the surface and the average height show similar

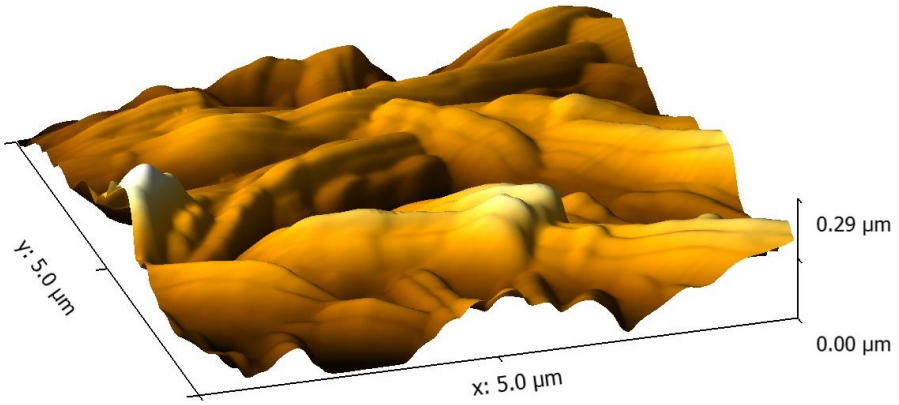

Figure 31: Result of the atomic force microscopy measurement of needle-like structures on a sample prepared at a substrate temperature of 172°C

Table 11: Data about the surface morphology gained from the atomic force microscopy measurements shown in figures 27 - 31
T_{sub} ... substrate temperature during deposition
σ_{rms} ... surface roughness (route mean squared)
h_{max} ... maximum detected height
h_{av} ... average height within the image (lowest detected point is 0 nm)
* ... surface roughness just from the highlighted area in figure 28

$\mathbf{T_{sub}}$ / °C	25	100	150	172 (middle)	172 (needles)
σ_{rms} / **nm**	1	10*	4	5	60
$\mathbf{h_{max}}$ / **nm**	10	300	50	40	400
$\mathbf{h_{av}}$ / **nm**	7	70	30	20	140

trends. Even though the trends are obvious the AFM image of the sample prepared at a substrate temperature of 100°C shows nucleated structures sticking out of the film up to thickness values of ∼300 nm. This is in accordance to pictures recorded by optical microscopy where on films prepared at substrate temperatures of 100°C and higher needle-like structures start to appear in all samples. Even though the surface roughness has been evaluated in a smaller area of the AFM measurements plotted in figure 28 (as described) the value is higher than the surface roughness values for the films prepared at higher substrate temperatures (150°C and middle of the sample at 172°C). This could either be caused by the growth mechanism of Alq(3) thin films at that substrate temperature or by the nucleated structures next to but also causing an increased surface roughness in the area where the value has been measured in the plot in figure 28. On the AFM image of the sample prepared at 100°C the structures causing the increase in surface roughness appear to be of

lateral sizes of ∼300 nm. At higher substrate temperatures (150°C) smaller structures of lateral sizes of ∼50 nm seem to affect the surface roughness in addition to the larger structures also occurring in the film prepared at 100°C substrate temperature. In the AFM image recorded in the middle of the sample prepared at the even higher substrate temperature of 172°C the smaller structures again disappeared and therefore, large lateral structures (∼500 nm) alter the surface roughness. The AFM measurements just investigate a very small area (25 μm^2) compared to the whole substrate (1 cm^2). Therefore, the data is not representative and the given values in table 11 could deviate from the integral values of the whole sample as the growth has been evaluated to be very inhomogeneous throughout the whole substrates by other techniques like optical microscopy or lattice phonon Raman spectroscopy (see sections 7.1 and 7.7 respectively).

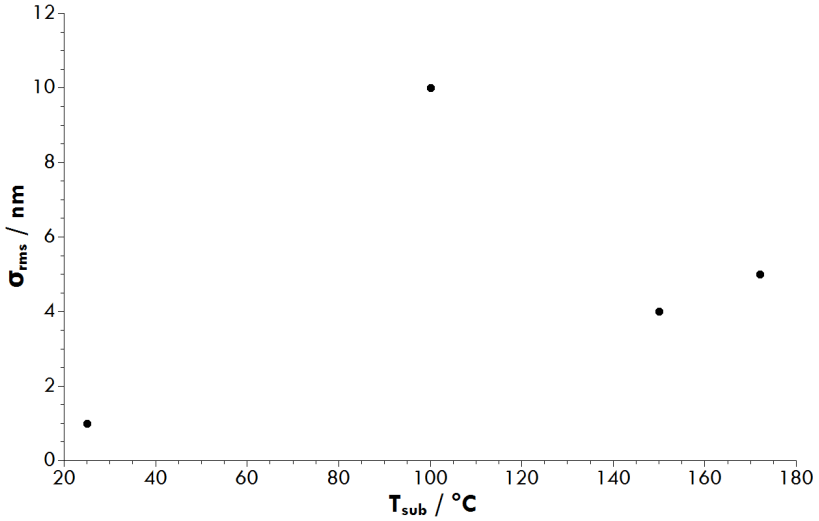

Figure 32: Surface roughness σ_{rms} vs. substrate temperature during deposition T_{sub} as evaluated from the atomic force microscopy measurements in figures 27-30

The behaviour of the surface roughness determined from the AFM measurements (for the data see table 11) can be found in figure 32 (compare to section 7.3).
The inhomogeneous surface roughness behaviour with increasing the substrate temperature during deposition evaluated from the AFM measurements considering also the data from the XRR measurements (see section 7.3) shows that the surface roughness increases with increasing the substrate temperature up to about 100°C (difference in XRR and AFM measurements). At even higher temperatures the surface

roughness decreases pretty rapidly (up to 140°C substrate temperature) and then starts to increase again slightly up to the point where desorption dominates the process of Alq(3) molecules sticking to the substrate surface. This just holds for regions where no nucleation of needle like structures has taken place. The inhomogeneity of the films and also the inhomogeneous nucleation of these needle-like structures makes it hard to get any representative values of the surface roughness. Despite that fact a similar behaviour of the surface roughness with respect to the substrate temperature during deposition to the trend reported in this thesis has been described to occur due to an isomeric transformation of the low temperature mer-isomer to the high temperature fac-isomer in a range of substrate temperatures of 90-120°C by Jian et al. [26]. As mentioned before many factors could influence the behaviour of the surface roughness with increasing substrate temperature during deposition [25], [26], [27], [32].

In all cases for substrate temperatures lower than 172°C the average surface height is lower than the nominal thickness of 100 nm. This leads to the conclusion that for these cases there is always a film underneath the surface structures investigated by the method of AFM.

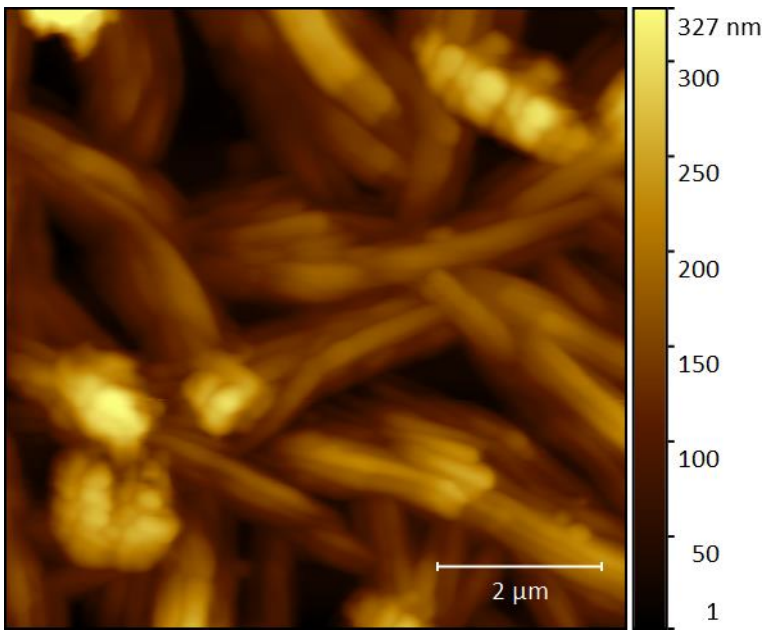

Figure 33: Result of the atomic force microscopy measurement of needle like structures on a sample prepared at a substrate temperature of 172°C

The average surface height of the area investigated by AFM on the sample prepared at a substrate temperature of 172°C (see figures 31 and 33 and table 11) has been evaluated to be 140 nm. As the nominal thickness was set to be 100 nm this allows to conclude that most probably the film consists of needle-like structures in the investigated region all the way from the surface down to the substrate. Presumably the substrate has still areas where no Alq(3) molecules are attached which could be caused either by the growing mechanism of these films or by the inhomogeneous temperature gradient on the substrate due to inhomogeneous thermal contact to the heated substrate holder (see section 6.2). Even though a levelling process has been performed on the images the high roughness could be a problem for that and therefore, also a reason for causing the high nominal thickness value on the sample prepared at $T_{sub} = 172°C$. Also the inhomogeneity of the sample prepared at a substrate temperature of 172°C (see figures 30 and 31) is so distinct that on different regions on the sample the surface roughness differs in a range of one order of magnitude.

An AFM image showing the height map of a part of the surface of a sample prepared at a substrate temperature of 172°C can be found in figure 33. It shows needle-like structures exhibiting a width of $\sim$1 μm and a length of $\sim$2 μm with voids in between. Further investigation reveals that these needles consist of even smaller needle-like structures of the size of $\sim$200 nm in width. Taking a look on the colour along these smaller needles (also see figure 31) makes it clear that the colour and therefore, the height does not change much along a needle. This leads to the conclusion that the needles mostly lie flat on the surface. This is in accordance with the needle growth stated in the cif-file from Brinkmann et al. [3] and the results from the GIXD-measurements (see chapter 7.6) where the $(0,\overline{1},1)$- and the $(0,\overline{1},0)$-plane were evaluated to be the most probable contact planes for crystal growth.

7.5 Specular X-ray diffraction (XRD)

Specular X-ray diffraction experiments have been performed on the same instrument as all XRR-measurements - the *PANalytical Empyrean* (see section 7.2). As in the XRR case all measurements have been performed with a non-reflecting Si block between the sample desk and the sample.

A series of samples has been investigated by specular XRD at angles from $2\Theta = 5°$ to $60°$. The resulting patterns can be found in figure 34.

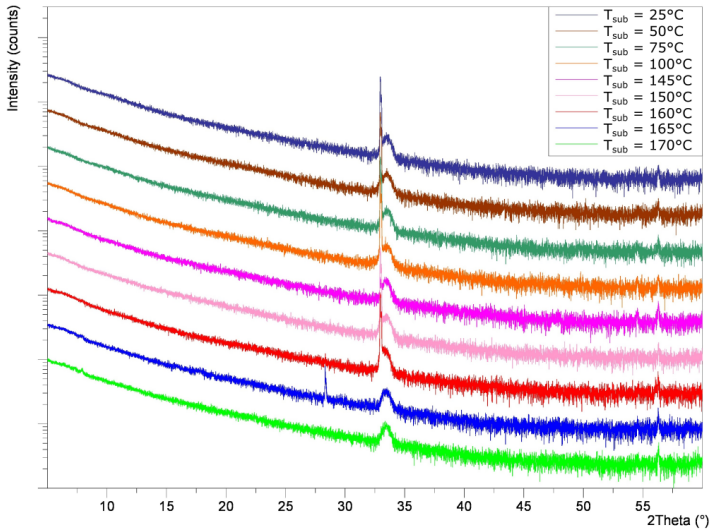

Figure 34: X-ray diffraction patterns for a series of samples ranging in substrate temperatures (T_{sub}) during deposition from room temperature up to 170°C in a waterfall plot

The data in figure 34 shows multiple peaks for all the spectra. All the spectra prepared up to substrate temperatures of 160°C show a combination of two close sharp peaks at $2\Theta = 32.95°$ and $2\Theta = 33.05°$. While the patterns of the two samples with the highest substrate temperatures do not show these two peaks all the spectra exhibit a broad peak at $2\Theta = 33.35°$. A peak of very low intensity appears at $2\Theta = 56.2°$ in all the measured curves. The sample prepared at a substrate temperature of 165°C shows also a peak at a 2Θ value of 28°. All the peaks in the 2Θ range around 33° can be attributed to the silicon 200-reflection [33] that can be observed as a combination of peaks in this region. The silicon 311-reflection could

be observed at an angle of $2\Theta = 56.1°$ [34] but this plane is tilted about an angle of ∼25° with respect to the (100) plane. The same holds for the silicon 111-reflection at 28.4° [34]. Due to that fact these peaks should not be observed in specular conditions on a Si(100) wafer despite running the detector in scanning line mode where it detects slightly off specular angles (see section 7.2). Therefore, this very weak peak at 56° and also the peak occurring at 28° in the pattern of the sample prepared at a substrate temperature of 165°C can be attributed to unwanted diffraction on the sample desk that can be detected when the sample lies on the sample desk unfavourably during the experiment. In conclusion none of the clear peaks mentioned above could be assigned to the Alq(3) films.
Multiple intensity variations are visible at lower 2Θ values below 10° but are very low in intensity. These fluctuations appear as peaks in the two samples prepared at the highest substrate temperatures. The peak at $2\Theta = 7.93°$ is visible in all the samples prepared at substrate temperatures higher than 150°C. The two samples with $T_{sub} = 165°C$ and $T_{sub} = 170°C$ show multiple bumps in this range including 2Θ values of 7.36° and 7.93° (see figure 35). The peaks at 7.36° and 7.93° could also be seen as broader but more intense peaks compared to the background in the XRR measurements (see section 7.3) and can be attributed to the Alq(3) layer (see section 7.6).

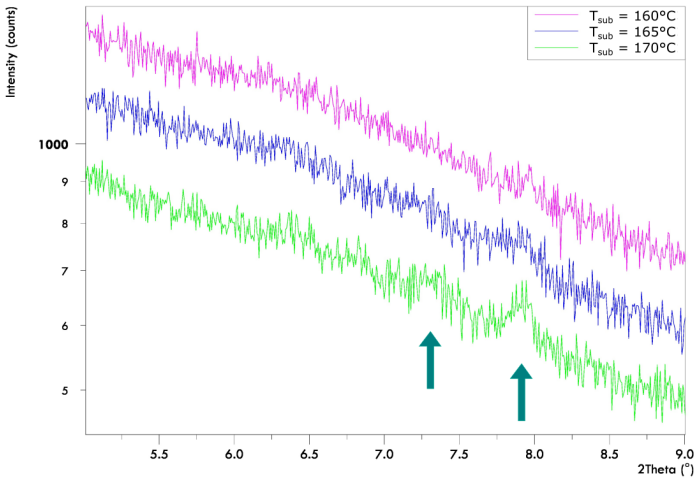

Figure 35: Zoom of the X-ray diffraction patterns (see figure 34) of samples ranging in substrate temperatures (T_{sub}) during deposition from 160°C to 170°C in a waterfall plot

7.6 Grazing incidence X-ray diffraction (GIXD)

Grazing incidence X-ray diffraction measurements have been performed at the synchrotron *Diamond* in Oxfordshire, UK. The wavelength used for all investigations has been set to $\lambda = 1$ Å. 3 samples have been investigated whereas the conversion from the real space diffraction pattern to reciprocal space has been performed by a "home-made" script. The intensities could then be mapped and compared to crystal structures from res-files with the help of the software *PyGid* [35]. For the α-phase data (cif and res-file from Brinkmann et al. [3]) only the most dominant peaks have been selected from the cif-file and only these are shown in all the spectra.

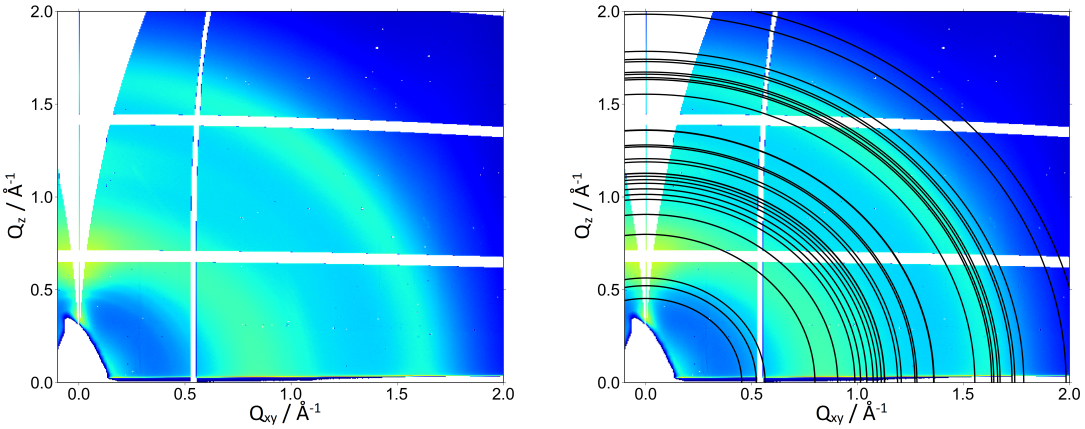

Figure 36: Grazing incidence X-ray diffraction pattern of a sample prepared at a substrate temperature of $T_{sub} = 150°C$ without (left) and with overlay of rings corresponding to the α-phase Alq(3) crystal structure (right)

Figure 36 shows the result of a GIXD measurement of a sample prepared at a substrate temperature of $T_{sub} = 150°C$. The reciprocal space-map shows two broad rings at $|Q| = 1.6$ Å^{-1} and $|Q| = 0.8$ Å^{-1} with a strong intensity peak in spectral conditions at $Q_z = 0.7$ Å^{-1} which is also smeared out to a ring at the respective absolute value of Q. Wang et al. [36] reported that an amorphous-like structure appearing in Alq(3) thin films deposited at room temperature shows exactly the two peaks at $|Q| = 1.6$ Å^{-1} and $|Q| = 0.8$ Å^{-1} in a specular XRD scan. The right picture in figure 36 shows that the overlayed black rings from the α-phase match the outer two smeared out rings. Also the innermost three vaguely visible rings at $|Q| = 0.46$ Å^{-1}, $|Q| = 0.525$ Å^{-1} and $|Q| = 0.57$ Å^{-1} match. The peak at $Q_z = 0.7$ Å^{-1} cannot be attributed to the α-phase. After further investigation also neither of the other crystalline phases of Alq(3) shows intensity peaks in the region around 0.7 Å^{-1}. As the GIXD measurement can be seen as a tool that

"counts" distinct distances occurring in the investigated system these broad ring structures can be attributed to an amorphous phase of Alq(3) where the respective intensity peaks in the GIXD map are dominant and correspond to distances in the structure. The broad ring structures then stand for no preferred orientation of the occurring patterns at dominant distances. The mer-Alq(3) molecule (see section 5.1) has roughly the shape of a triangular prism with a side length of about 9 Å on the triangular side and a depth of about 5 Å [3]. Therefore, this amorphous phase could be described as dominantly standing Alq(3) molecules as $Q_z = 0.7$ Å^{-1} corresponds to a distance of about 9 Å.

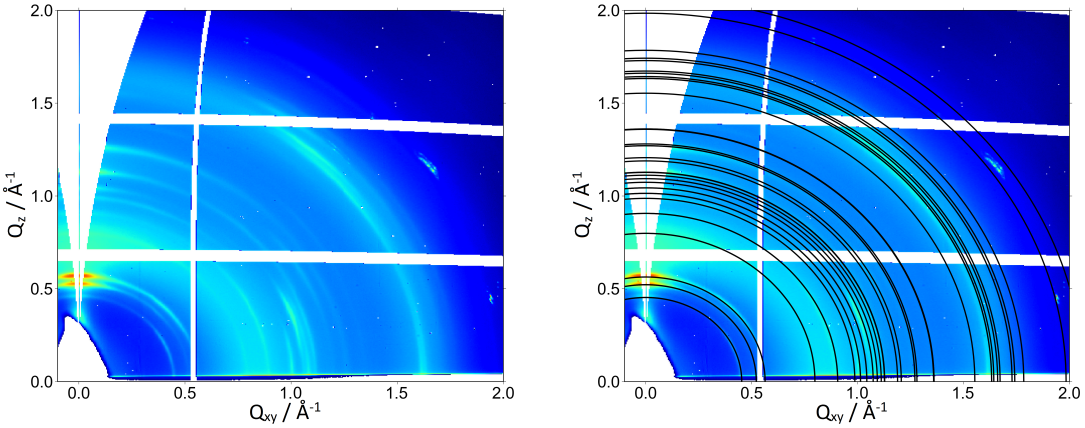

Figure 37: Grazing incidence X-ray diffraction pattern of a sample prepared at a substrate temperature of T_{sub} = 165°C without (left) and with overlay of rings corresponding to the α-phase Alq(3) crystal structure (right)

Figure 37 shows the GIXD pattern of a sample prepared at a substrate temperature of 165°C. A distinct ring structure is visible in the reciprocal space map. The overlay with the α-phase of Alq(3) (see figure 37 right) shows a good agreement of the rings corresponding to the crystal structure of the α-phase of Alq(3) with the measured GIXD pattern although a smeared out peak at $Q_z = 0.7$ Å^{-1} is still visible (compare to figure 36). Also an elevated background intensity in the $|Q|$-range of 0.5 Å^{-1} to 1.7 Å^{-1} can be observed. This can be explained by co-existing α- and amorphous phases on the sample prepared at a substrate temperature of 165°C.

The measured ring-like intensity maxima appear to be a little distorted compared to the theoretical rings corresponding to the crystalline Alq(3)-α-phase. The theoretical ring positions at low scattering vectors (0.45 Å^{-1}, 0.523 Å^{-1} and 0.564 Å^{-1}) make it possible to compare these to the measured positions and give a deviation of the measured positions for the components Q_z and Q_{xy} of the scattering vector.

$$\Delta Q_z = +0.005 \text{ Å}^{-1}$$
$$\Delta Q_{xy} = -0.003 \text{ Å}^{-1}$$

These deviations are probably caused by the alignment/positioning interfering with the construction of the 2D-detector but do not affect the qualitative analysis that is done on basis of the GIXD results in this work.

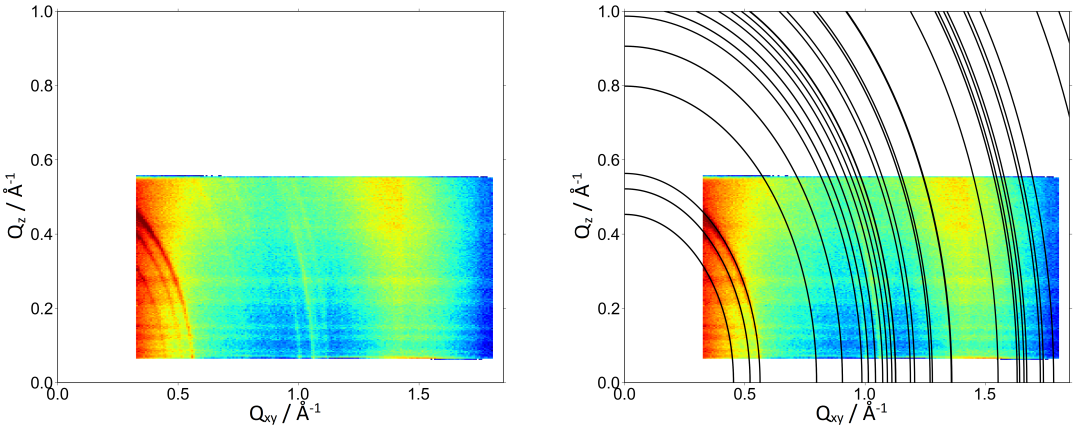

Figure 38: Grazing incidence X-ray diffraction pattern of a sample prepared at a substrate temperature of T_{sub} = 173°C without (left) and with overlay of rings corresponding to the α-phase Alq(3) crystal structure (right)

Figure 38 shows the GIXD pattern of a sample prepared at a substrate temperature of T_{sub} = 173°C in a smaller area in reciprocal space compared to the patterns in figures 36 and 37. This difference comes from the use of a different detector in this case. While the samples prepared at substrate temperatures of T_{sub} = 150°C and T_{sub} = 165°C have been investigated by a 2D-detector the sample prepared at a substrate temperature of T_{sub} = 173°C has been investigated with a 1D-detector which has been moved to collect a 2D-image. The rings corresponding to the α-phase of Alq(3) show good accordance with the intensity landscape of the

GIXD pattern up to $|Q|$-values of 1.3 Å^{-1}. At about $|Q| = 1.5$ Å^{-1} a broad peak occurs that cannot be connected to the α-phase. In this range in reciprocal space peaks corresponding to the β-phase of Alq(3) could occur but as there is no other evidence and also other β-phase lines cannot be observed this broad peak is not attributed to this phase. Due to the broadness of the peak an amorphous content (though shifted compared to the other samples - see figures 36 and 37) could be present also in the film prepared at a substrate temperature of $T_{sub} = 173°C$.

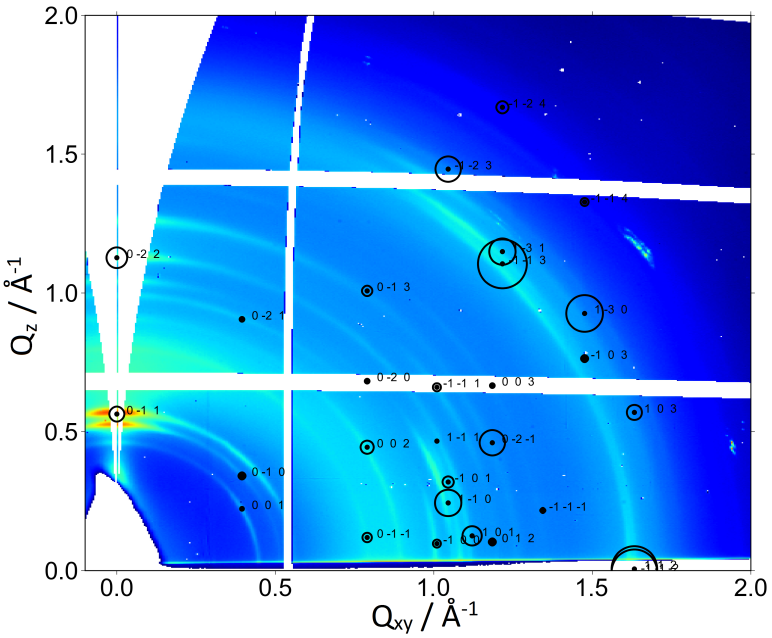

Figure 39: Grazing incidence X-ray diffraction pattern of a sample prepared at a substrate temperature of 165°C with overlayed peaks and structure factors of the Alq(3) α-phase for the $(0,\bar{1},1)$-orientation

The GIXD pattern in figure 37 which agrees with the calculated rings of the α-phase of Alq(3) allows to overlay it with structure factors and miller indices corresponding to the α-phase occurring in certain orientations. Figures 39, 41 and 44 show the reciprocal space map of figure 37 with the α-phase overlay of the given orientations. Figures 40, 42 and 43 show sketches of Alq(3) molecule stacking in an α-phase crystal with respect to a plane drawn into the sketch in the corresponding orientation. The GIXD patterns have been plotted and evaluated with the software *PyGid* The sketches of the molecule stacking have been drawn with *Mercury*.

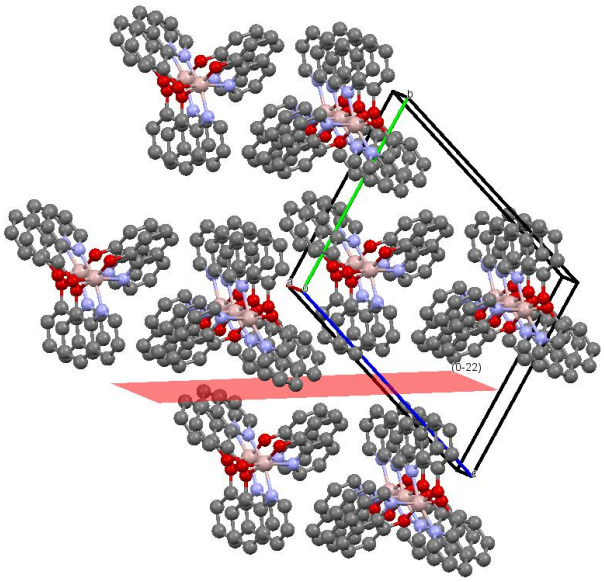

Figure 40: Sketch of the stacking of Alq(3) molecules in the α-phase for the (0,$\bar{1}$,1)-orientation (plane drawn in red)

The GIXD map in figure 37 shows the most prominent peak at a scattering vector of $Q_z = 0.57$ Å^{-1}. This peak has also been visible in the XRR and XRD measurements on samples prepared at high substrate temperatures (see sections 7.3 and 7.5). It corresponds to the spectral peak of the (0$\bar{1}$1)-reflection. An overlay of the theoretical peak positions with structure factors of an α-phase Alq(3)-crystal in (0$\bar{1}$1)-orientation with the measured pattern (see figure 37) in the background is shown in figure 39. Figure 39 shows the stacking of Alq(3) molecules together with the unit cell axes and a (0$\bar{1}$1)-plane as a representative surface where the molecules could stick to. The overlay shows that all the shown peaks lie in regions where intensity maxima are visible in the GIXD map. The molecule stacking (figure 40) shows that the (0,$\bar{1}$,1)-orientation is favourable for stacking because the lattice could start from such a flat surface without any deviation of the ordinary structure.

Another very intense peak in the GIXD map of figure 37 lies at a scattering vector of $Q_z = 0.52$ Å^{-1} (also see sections 7.3 and 7.5). This peak is attributed to the (0,$\bar{1}$,0)-reflection. Figure 41 shows the corresponding overlayed GIXD map and the possible stacking of Alq(3) molecules is given in figure 42. This leads to the conclusion that the (0,$\bar{1}$,0)-orientation is not as likely to occur starting from the surface of the substrate (flat plane - silicon oxide). The growth from this contact

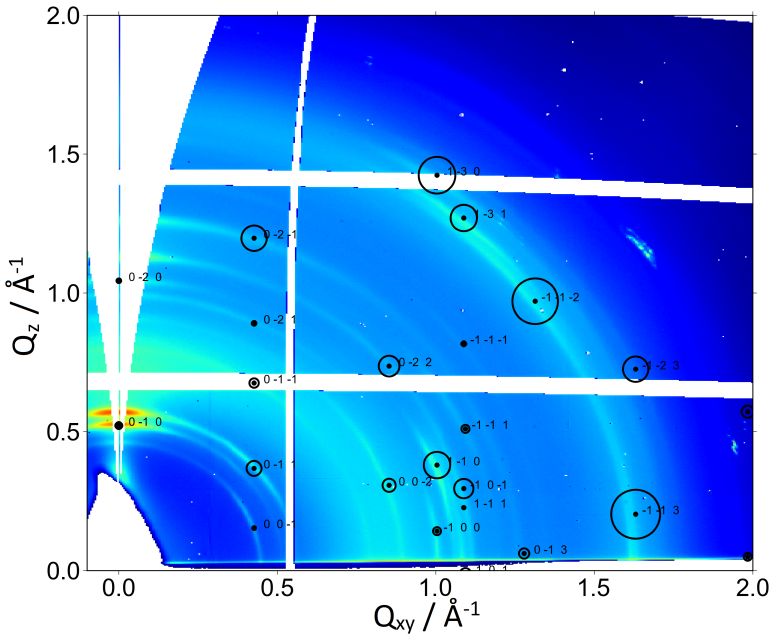

Figure 41: Grazing incidence X-ray diffraction pattern of a sample prepared at a substrate temperature of 165°C with overlayed peaks and structure factors of the Alq(3) α-phase for the $(0,\bar{1},0)$-orientation

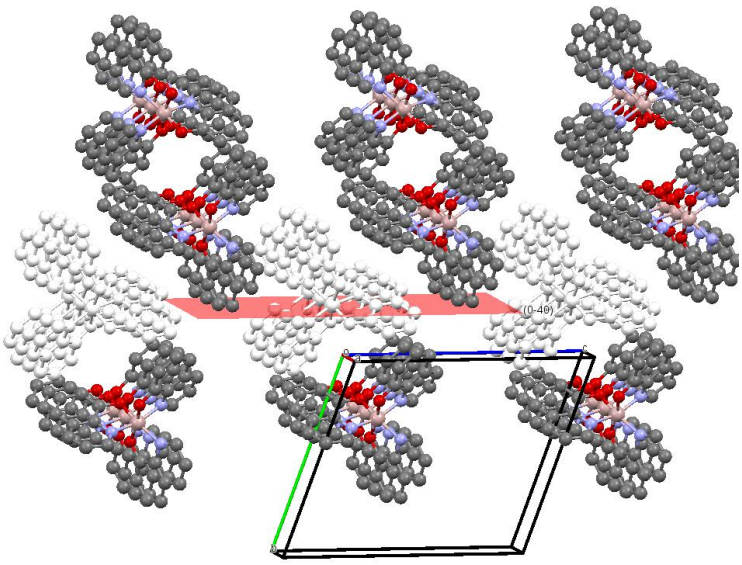

Figure 42: Sketch of the stacking of Alq(3) molecules in the α-phase for the $(0,\bar{1},0)$-orientation (plane drawn in red); white molecules intersect the plane

plane causes defects as the structure would have to deviate from the ideal α-phase structure if the crystal would grow in the (0,$\overline{1}$,0)-orientation. All peaks of this orientation occur in regions where increased intensity is visible in the GIXD pattern. Therefore, the structure is likely to occur in layers above other Alq(3) structures causing defects in the film.

From looking at the stacking of Alq(3) molecules another orientation is very likely to occur due to the fact that no voids or interstitial structures remain as the Alq(3) molecules stick to a surface from the (0,0,1)-plane as the contact plane (see figure 43). Therefore, the GIXD map of a sample prepared at a substrate temperature of T_{sub} = 165°C is shown with an overlay of the calculated peak positions and structure factors of an Alq(3) α-phase crystal in (0,0,1)-orientation. All the peaks lie in regions of increased intensity in the measured data whereas the low intensity specular (0,0,1)-reflection and the specular (0,0,2)-reflection are also visible.

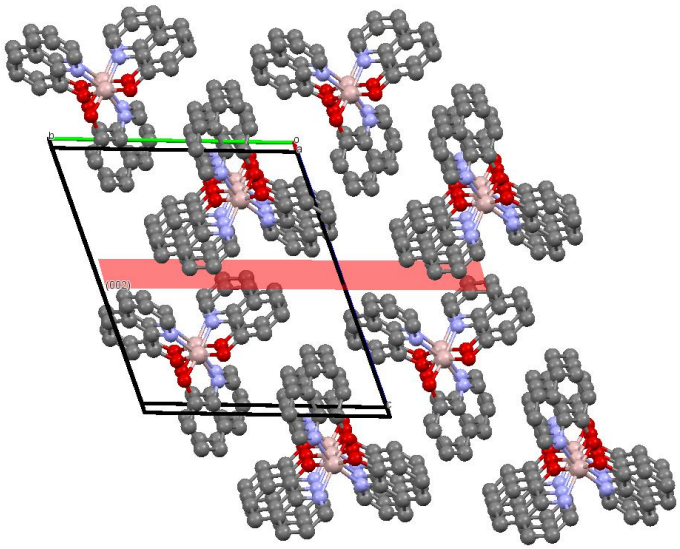

Figure 43: Sketch of the stacking of Alq(3) molecules in the α-phase for the (0,0,1)-orientation (plane drawn in red)

In specular direction also the peaks corresponding to the (0,2,1)- and the (0,1,1)-families are visible in the measured data. Despite that fact the peaks corresponding to the (0,$\overline{1}$,1)- and the (0,$\overline{1}$,0)-orientation are distinctively prominent. These orientations are therefore, evaluated to be the two main orientations of growth on the samples prepared at elevated substrate temperatures (above ∼160°C) whereas

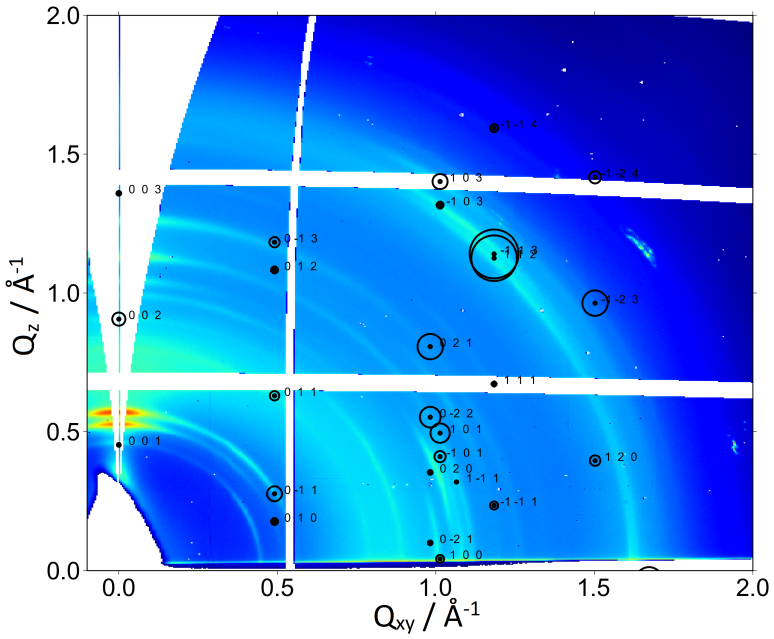

Figure 44: Grazing incidence X-ray diffraction pattern of a sample prepared at a substrate temperature of 165°C with overlayed peaks and structure factors of the Alq(3) α-phase for the (0,0,1)-orientation

the (0,$\overline{1}$,1)-orientation is the main orientation for surface growth on the very flat ($\sigma_{rms} \approx 0.5$ nm) silicon/silicon oxide substrates.

The symmetric smearing of all the intensity peaks in the GIXD maps is very distinct. Therefore, it can be said that the orientations present on the samples and evaluated in this work are not very defined and limited to the orientation given from the specular reflection but also seem to occur in a slightly tilted configuration.

The AFM measurements (see section 7.4) showed that the needle-like structures exhibit a relatively flat surface on top. Therefore, the needles appear to lie flat on the substrate. Considering the main orientations obtained from GIXD to be α-crystallites growing from (0,$\overline{1}$,1)- and (0,$\overline{1}$,0)-planes this is in accordance with the needle growth stated in the cif-file of Brinkmann et al. [3]. Alq(3) molecules are therefore, standing on these planes (see stacking in figures 40 and 42) and seem to be stacked closely along the needles.

7.7 Lattice phonon Raman spectroscopy

At the university of Bologna in the institute of industrial chemistry a measurement set-up for micro-Raman spectroscopy has been used to investigate the crystallinity of the prepared films. An optical microscope (*Olympus BX40*) connected to a *Jobin Yvon T64000* Raman spectrometer allows to place samples on the optical stage of the microscope so that a certain point on the sample can be focused with several different objectives (10x, 20x, 50x, 100x). For the 100x objective the spatial resolution is in the range of about 1 μm and a theoretical field depth in the range of 7 to 25 μm is obtained [20]. All the spectra shown cover the low frequency region of the lattice phonons (10 - 260 cm^{-1}). The excitation wavelength from a Krypton laser has been tuned to 647.1 nm, an excitation energy sufficient to get signal from the lattice phonons and to avoid background fluorescence from the sample in this low wavenumber region. The outcoming power of the laser was reduced to be kept at $\sim$450 mW.
With an excitation wavelength of 514 nm it was also possible to get signal from the powder samples but fluorescence raised the background intensity in a way that the signal was very small on top of the background. Also laser light of larger wavelengths (f.e. 785 nm) has been tried but for these excitation energies it was not possible to get signal of the Alq(3) samples in the phonon region with the set-up at hand.
Calibration of the spectra was done with the help of a Neon lamp. The energies of the Ne lines were taken from the NIST webpage (National Institute of Standards and Technology) [37]. Calibrated spectra with the 100x objective on a blank silicon substrate have been recorded after each measurement cycle and the respective spectrum is shown in every figure of Raman spectra as a reference.

Raman spectra measured on samples prepared at substrate temperatures of 100°C and 140°C are shown in figure 45. Comparison of the spectra on the samples with deposited film with the spectrum of the blank substrate shows that the intensity is increased in the low wave number region (below 150 cm^{-1}) due to the Alq(3) film. A peak at 307 cm^{-1} can be attributed to the substrate. Also in the region from 150 cm^{-1} to 260 cm^{-1} a few low intensity peaks can be observed. Therefore, all the following spectra on thin films will be plotted in the wave number region of 9 cm^{-1} to 260 cm^{-1}. The spectrum measured on the "big crystal needles" has a similar behaviour as the spectrum measured on the "edge structure" but the trend occurs to be much more pronounced.

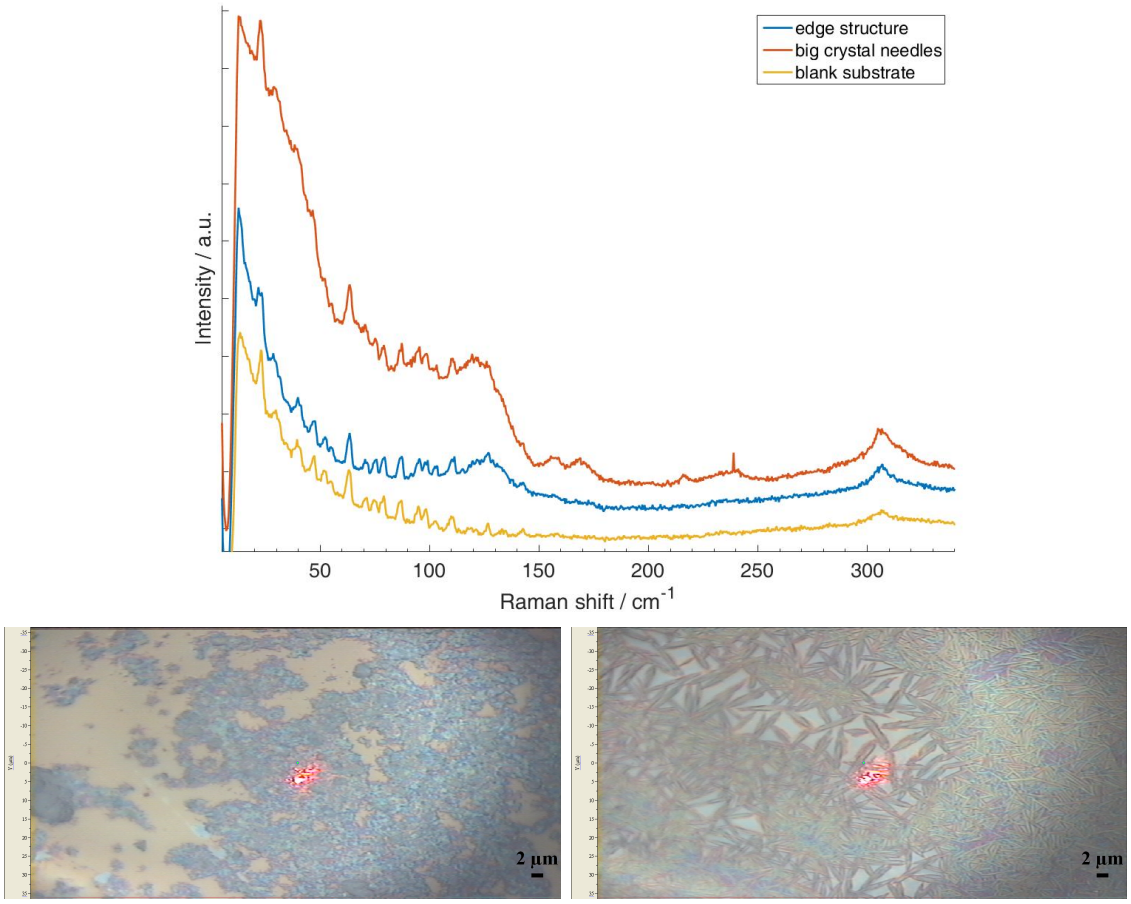

Figure 45: Raman spectra and corresponding optical microscopy pictures at different spots on samples prepared at substrate temperatures T_{sub} = 100°C (edge structure - left) and T_{sub} = 140°C (big crystal needles - right)

Raman spectra on different spots on a sample prepared at a substrate temperature of 150°C are shown in figure 46. The spectrum measured on the spot where needles can be observed in the optical microscope shows a very similar behaviour as the spectrum of the "big crystal needles" in figure 45. The spectrum measured in the middle of the film does not show much difference compared to the spectrum measured on the blank substrate except a slightly increased intensity at very low wave numbers below 30 cm^{-1}.

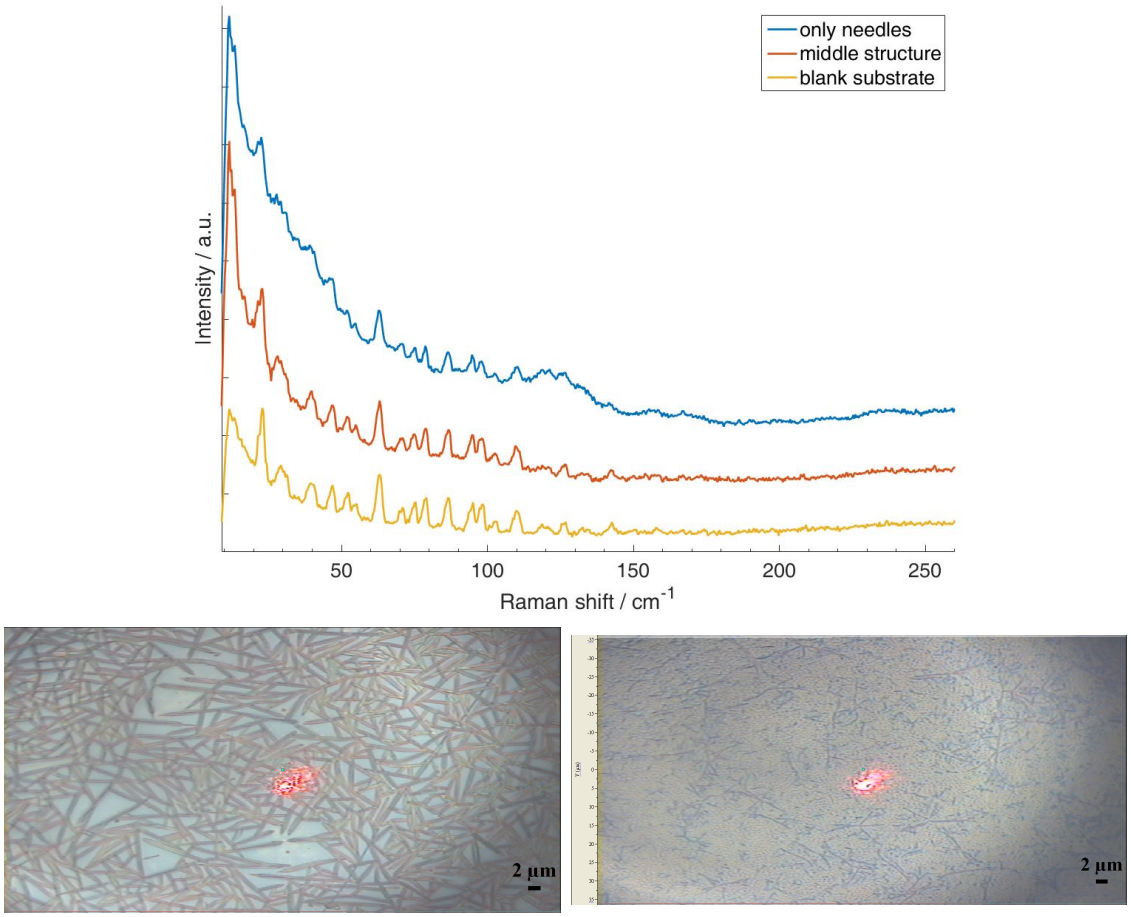

Figure 46: Raman spectra and corresponding optical microscopy pictures (only needles - left; middle structure - right) at different spots on a sample prepared at a substrate temperature of $T_{sub} = 150°C$

The Raman spectra measured on a sample prepared at a substrate temperature of 172°C are shown in figure 47. As the spectra in figures 45 and 46 the spectra measured on structures on Alq(3) thin films show broad increased intensity in the wave number region below 150 cm^{-1} and several small bumps in intensity in the range between 150 cm^{-1} and 260 cm^{-1}.

From literature [11] Raman spectra of all the crystalline polymorphs of Alq(3) are available for Raman shifts in the range of ∼70 cm^{-1} up to ∼600 cm^{-1} in wave numbers. The phonon-part has not been studied yet. This is especially true for thin films where also not much can be found for the part of the spectrum that corresponds to the internal modes. Rajeswaran et al. [11] do not even show the whole spectrum (see low wave numbers) for the β-phase of Alq(3) below 100 cm^{-1}. From Brinkmann

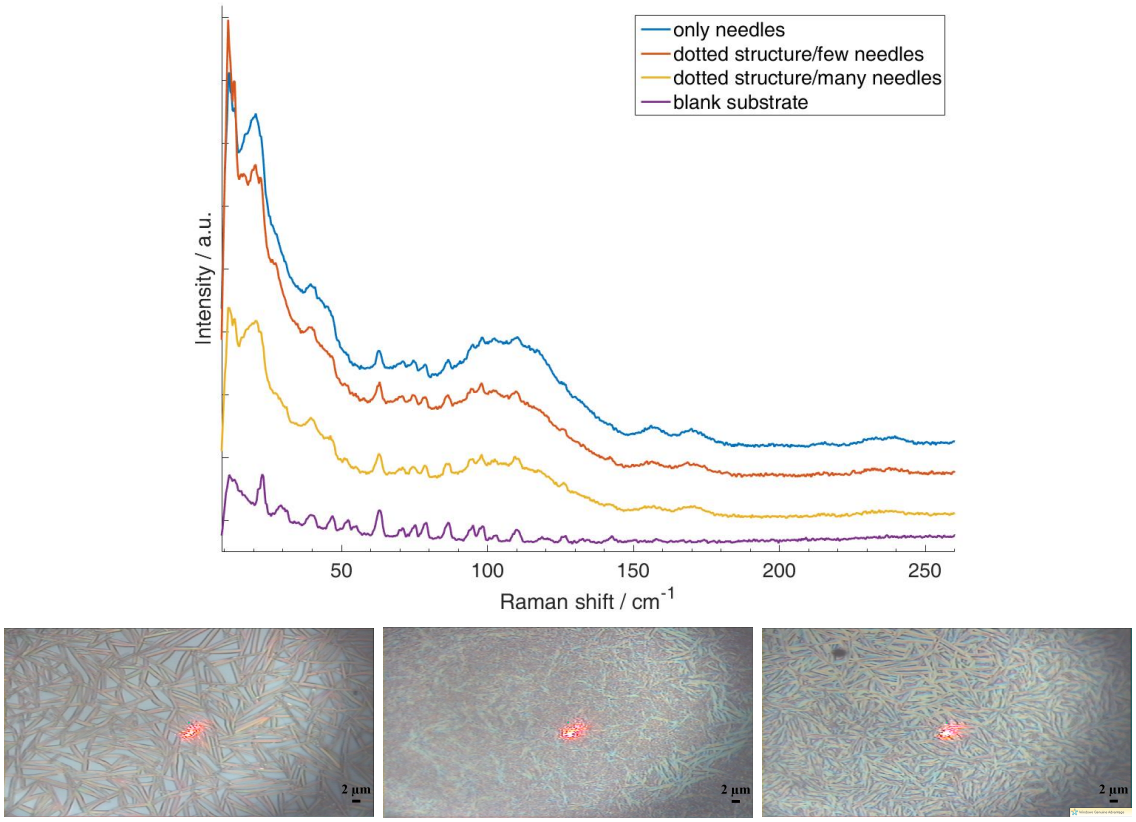

Figure 47: Raman spectra and corresponding optical microscopy pictures (left to right as listed in the legend) at different spots on sample 30 (T_{sub} = 173°C)

et al. [3] it was known that β-crystals could be obtained together with α-crystals by recrystallisation from Acetone. These would stick out as the α-crystals show needle-shape and the β-crystals should be larger and flat. The powder from *Sigma-Aldrich* has then been used as the source for recrystallisation in Acetone. After investigation of the recrystallised products it was found that only larger needles probably containing the α-phase appeared. Investigation of the as received powder from *Sigma-Aldrich* and the recrystallised needles by the micro-Raman technique gave the spectra shown in figure 48.

The two spectra shown in figure 48 show similar behaviour for both the investigated samples. Three peaks in the range between 20 cm^{-1} and 40 cm^{-1} appear to be better resolved in case of the Alq(3) sample after recrystallisation. From XRPD it is known that the powder from Sigma Aldrich contains the α-phase. During the recrystallisation process the α-crystals have time to grow. Raman peaks appear more distinct in bigger crystals as is true for all the peaks in the spectrum and therefore,

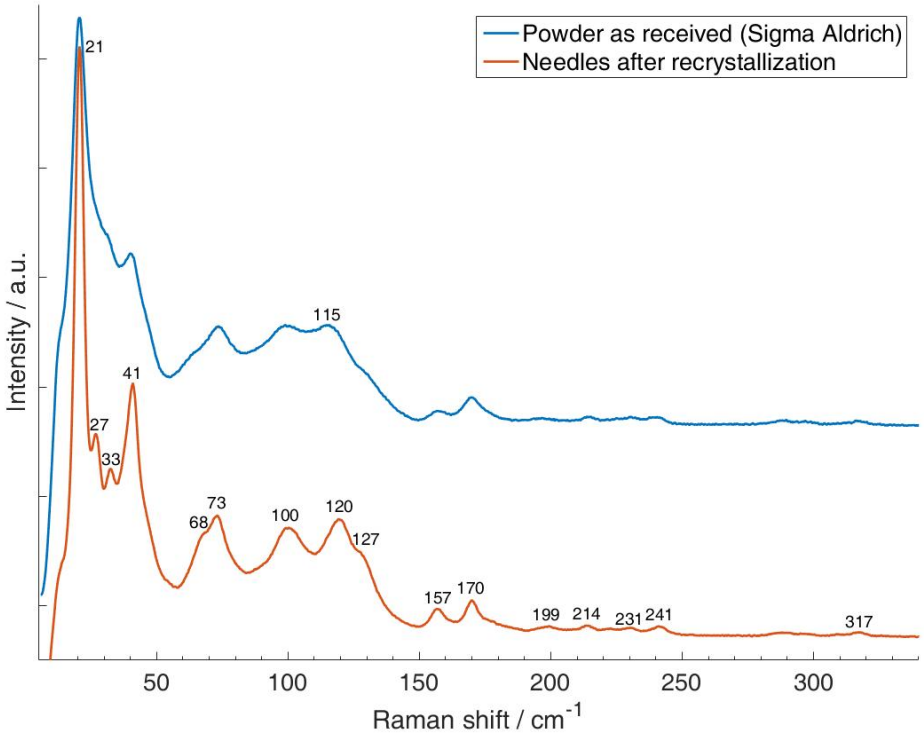

Figure 48: Raman spectra in the phonon region of the as received powder from *Sigma-Aldrich* and the recrystallised needles in a waterfall plot (peaks labelled with the corresponding wave numbers)

the spectral structures mentioned above can get visible from what we see as a shoulder of the respective peak in the spectrum of the as received powder. The peak at 115 cm^{-1} in the spectrum recorded on the powder as received from *Sigma-Aldrich* is shifted towards a higher wave number of 120 cm^{-1} in the spectrum recorded on needles after the recrystallisation process mentioned above. As all the other peaks appear in a region of ± 1 cm^{-1} of the wave number values given in figure 48 this can be attributed to polarization and anisotropy effects affecting the recording of the different spectra.

The recorded spectra make it possible to compare the powder spectrum to a thin film spectrum together with a spectrum recorded on the blank substrate. This is shown in the waterfall plot in figure 49.
The comparison in figure 49 shows clearly that the broadly increased intensity in the spectra of the Alq(3) thin film samples below 150 cm^{-1} can be ascribed to the

Alq(3) film and not the substrate. Also in the higher wave number region small bumps in intensity appear where the intensity also peaks in the powder spectrum. All smaller structures on top of the broader features from the Alq(3) phonons come from the Si/SiOx substrate as the depth in which the laser beam can penetrate into the sample can be of the order of micrometers. All the recorded spectra for film and powder samples show good accordance when compared to the work done by Rajeswaran et al. [11] for the α-phase data in the overlapping region of wave numbers investigated.

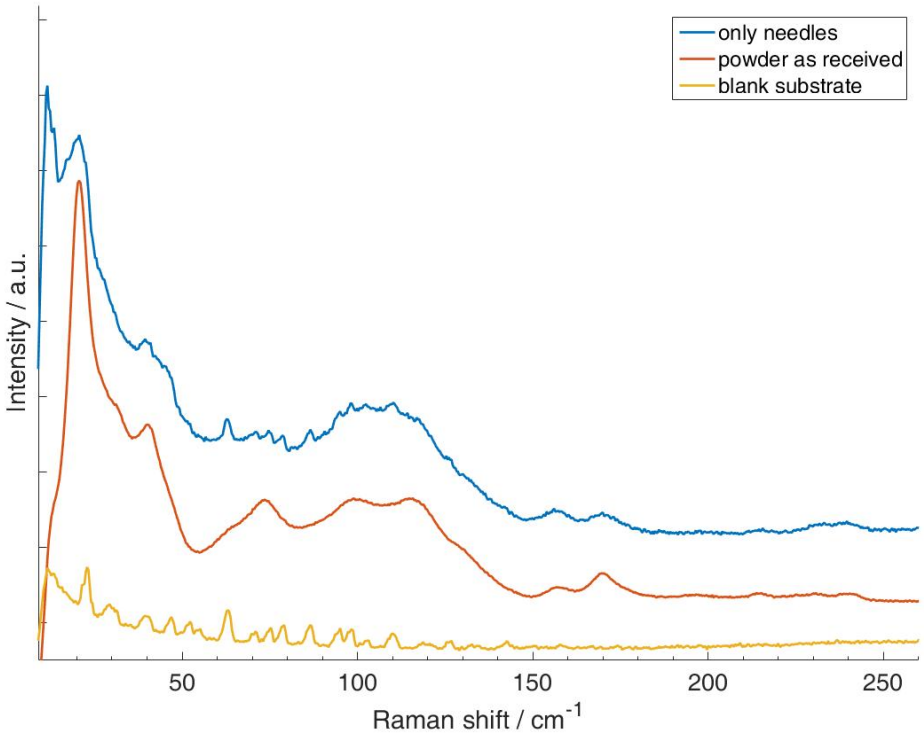

Figure 49: Raman spectra in the phonon region of the as received powder from *Sigma-Aldrich*, a spectrum recorded on needles on a thin film sample (see figure 47) and the blank Si/SiOx substrate in a waterfall plot

All in all, it has been possible to show that investigation of the needle-like structures gives signal in the lattice phonon region of the Raman spectra and investigation of all the regions where no needles appear does not. This leads to the conclusion that the needles show crystalline character and the other structures (e.g. the films deposited at substrate temperatures close to room temperature) are amorphous.

8 Conclusion

Alq(3) thin films have been deposited via physical vapour deposition on silicon/silicon oxide substrates at various substrate temperatures ranging from room temperature (25°C) to a temperature where desorption dominates the process of molecules sticking on the substrate surface (173°C).

8.1 Surface roughness behaviour

From X-ray reflectivity and atomic force microscopy measurements the surface roughness has been evaluated to exhibit an increasing trend in the majority of the range of investigated substrate temperatures. AFM scans show that the surface roughness first increases exhibiting structures of lateral sizes of ∼400 nm up to substrate temperatures of ∼100°C. At that point smaller structures having lateral sizes of ∼50 nm decrease the surface roughness. At substrate temperatures of about 150°C the small structures start to disappear again at the cost of the larger bumps growing in lateral size (and in height). The XRR measurements show a similar trend but with different temperature regions where a decrease in surface roughness occurs. The trend of surface roughness decrease in a range of 90-120°C has been reported by Jian et al. [26]. In reference [26] the explanation for this behaviour is a transformation between the low temperature meridional isomer to the high temperature facial isomer in this temperature range. In literature this change has been reported to happen at much higher temperatures of ∼395°C as the transition from the crystalline α- to γ-phase by Brinkmann et al. [3] in solid state. That this transition can be observed at lower temperatures (close to or even below room temperature) in solution [9] has been a reason for the explanation of the inhomogeneous surface roughness behaviour with increasing substrate temperature in reference [26]. Despite reference [26] also other different trends of the surface roughness with increasing substrate temperature have been reported [25], [27], [32]. Amongst other factors the substrate seems to play an important role in the surface roughness behaviour as various different substrates used in the mentioned works gave these different trends.

8.2 Crystallinity of the samples

At elevated substrate temperatures (>100°C) needle-like structures start to appear inhomogeneously distributed throughout the whole substrate. These structures were more likely to occur at spots close to where the substrate was attached to the heated substrate holder by metal springs. It could not be evaluated whether this inhomogeneous nucleation can be attributed to the inhomogeneous temperature gradient on the substrate occurring due to inhomogeneous thermal contact between the substrate holder and the substrate or to the growth behaviour of Alq(3) itself at elevated substrate temperatures.

Films deposited at substrate temperatures from room temperature up to approximately 100°C have been shown to have amorphous character exhibiting low surface roughness (1 nm - 5 nm for 100 nm thick samples). The presumption of Brinkmann et al. [3] that Alq(3) thin films deposited at room temperature show amorphous character has been verified by grazing incidence X-ray diffraction and lattice phonon Raman measurements. The amorphous phase has been evaluated to consist of preferentially standing Alq(3) molecules by GIXD.

GIXD measurements showed that the crystallinity of the samples increases with increasing the substrate temperature above ∼150°C. The needle-like structures mentioned above were found to be of crystalline phase and exhibit the structure of the crystalline polymorph α of Alq(3). Lattice phonon Raman spectra show the clear difference between the amorphous flat and the crystalline rough surface areas. From literature research it has been found that lattice phonon Raman spectra have been measured on Alq(3) thin film samples down to a film thickness of 50 nm for the first time in this work.
GIXD measurements make it possible to evaluate three dominant orientations of the Alq(3) α-phase on the samples. The most dominant one being the $(0,\overline{1},1)$-orientation also being the dominant form of α-phase growth on the substrate surface. Next in intensity and more probably growing on top of other Alq(3) structures than directly on the substrate surface the $(0,\overline{1},0)$-orientation occurs on the samples causing defects in the thin film. With weak intensity but showing a favourable packing pattern the (0,0,1)-orientation has also been evaluated to appear on the Alq(3) thin film samples prepared at substrate temperatures close to desorption.

8.3 Challenges in investigation

The results of the study of the surface roughness with on the one hand the integral technique of XRR and on the other hand with the very locally limited technique of AFM appears to be difficult as also in literature there seems to be no uniform theory about the surface roughness behaviour of Alq(3) thin films as a function of substrate temperature during deposition [25], [26], [27], [32]. Furthermore, the presence of both the crystalline needles and the amorphous film on all the samples prepared at substrate temperatures above 100°C makes this investigation even more difficult.
The explanation by Jian et al. [26] that the increased surface roughness in the substrate temperature range between 90°C and 120°C is being caused by a transition from meridional to facial Alq(3) would induce that the higher substrate temperature samples should exhibit meridional phase structures (δ or γ). However, the crystalline Alq(3) in films deposited at high substrate temperatures close to where desorption dominates the process of Alq(3) molecules sticking to the surface show strong indications of α-phase Alq(3) being present in the needle-like structures examined by GIXD and lattice phonon Raman measurements. This corresponds to the meridional isomer of Alq(3) [2]. The amorphous structures co-existing with the needles on some samples could not be evaluated with respect to their isomeric conformation.

Alq(3) has been the first active layer material of organic light-emitting diodes and has been studied widely since. Crystalline Alq(3) has been a promising outlook for the improvement of organic LEDs due to the blue shifted luminescence spectra of some of the crystalline phases [9]. In addition to the α-phase not being one of these structures the measured surface roughness values for the crystalline samples in this work would be detrimental for the preparation of real devices. This is also one reason why the usage of molecular glasses/amorphous layers in real device structures [38] is of great scientific interest.

List of Tables

1 Overview of the relation between the Alq(3) isomers and the polymorphs 6
2 Properties of the Alq(3) (Tris-(8-hydroxyquinolie)aluminum) powder used as the source for evaporation 13
3 Thermal conductivity values of the materials that the evaporation cells used in the experiments are made of 18
4 Properties of the Si wafers used as substrates 24
5 Parameters obtained from the fit of the measured X-ray reflectivity data from a cleaned substrate 27
6 Parameters obtained from the fit of the measured X-ray reflectivity data from an uncleaned substrate 27
7 List of samples with the frequency shift on the quartz microbalance (Δf) and the thickness value obtained by X-ray reflectivity 30
8 List of samples prepared at substrate temperatures T_{sub} 30
9 Properties of the optical microscope of the institute used to investigate the thin films 32
10 List of roughness values for the different samples evaluated from the slopes in figure 24 40
11 Data about the surface morphology gained from the atomic force microscopy measurements shown in figures 27 - 31 45

List of Figures

1 Chemical structure of a Tris(8-hydroxyquinolinato)aluminium (Alq(3)) molecule 5
2 Sketch of the meridional and facial isomer of the Alq(3) molecule . . 6
3 Sketch for the visualisation of diffraction on Bragg planes 9
4 Sketch of different scattering mechanisms on basis of energy levels . . 11
5 X-ray powder diffraction pattern of the as received powder from *Sigma-Aldrich* 13
6 Sketch of the vacuum chamber used for the physical vapour deposition process 15
7 Pictures of the evaporation cells used for the physical vapour deposition process 16
8 Sketch of the sample holder (front view) 17
9 Sketch of the sample holder (side view) 17
10 Deposition rate vs. temperature for the Brass Knudsen cell (first cycle) 19
11 Deposition rate vs. temperature for the Brass Knudsen cell (second cycle) 20
12 Deposition rate vs. temperature for the steel Knudsen cell 20
13 Heating power vs. source temperature for the steel Knudsen cell . . . 21
14 Deposition rate vs. temperature for the glass evaporation cell 22
15 Result of the X-ray reflectivity measurement of a cleaned substrate . 26
16 Result of the X-ray reflectivity measurement of a uncleaned substrate 27
17 Microscopy pictures of a sample prepared at a substrate temperature of $T_{sub} = 100°C$ 32
18 Microscopy pictures of a sample prepared at a substrate temperature of $T_{sub} = 150°C$ 33
19 Microscopy pictures of a sample prepared at a substrate temperature of $T_{sub} = 172°C$ 34
20 Microscopy pictures of a sample prepared at a substrate temperature of $T_{sub} = 173°C$ 34
21 Photo of the diffractometer used for all X-ray reflectivity and specular X-ray diffraction measurements 36
22 Results of X-ray reflectivity measurements on a series of samples . . . 37
23 Critical angles of the samples of which the X-ray reflectivity data is shown in figure 22 39

24 $\ln(Iq^4)$ vs. q^2 for Alq(3)-films shown in figure 22 40
25 Surface roughness σ_{rms} vs. substrate temperature during deposition T_{sub} gained from the X-ray reflectivity measurements 41
26 Result of an X-ray reflectivity measurement on a sample prepared at a substrate temperature of 165°C 42
27 Result of the atomic force microscopy measurement of a sample prepared at a substrate temperature of 25°C 43
28 Result of the atomic force microscopy measurement of a sample prepared at a substrate temperature of 100°C 43
29 Result of the atomic force microscopy measurement of a sample prepared at a substrate temperature of 150°C 44
30 Result of the atomic force microscopy measurement in the middle of a sample prepared at a substrate temperature of 172°C 44
31 Result of the atomic force microscopy measurement of needle-like structures on a sample prepared at a substrate temperature of 172°C 45
32 Surface roughness vs. substrate temperature during deposition as evaluated from atomic force microscopy 46
33 Result of the atomic force microscopy measurement of needle like structures on a sample prepared at a substrate temperature of 172°C 47
34 X-ray diffraction patterns for a series of samples ranging in substrate temperatures (T_{sub}) during deposition from room temperature up to 170°C in a waterfall plot 49
35 Zoom of the X-ray diffraction patterns (see figure 34) 50
36 Grazing incidence X-ray diffraction pattern of a sample prepared at a substrate temperature of $T_{sub} = 150$°C 51
37 Grazing incidence X-ray diffraction pattern of a sample prepared at a substrate temperature of $T_{sub} = 165$°C 52
38 Grazing incidence X-ray diffraction pattern of a sample prepared at a substrate temperature of $T_{sub} = 173$°C 53
39 Grazing incidence X-ray diffraction pattern of the $T_{sub} = 165$°C sample with peaks corresponding to α-phase Alq(3) in $(0,\overline{1},1)$-orientation 54
40 Sketch of the stacking of Alq(3) molecules in the α-phase for the $(0,\overline{1},1)$-orientation 55
41 Grazing incidence X-ray diffraction pattern of the $T_{sub} = 165$°C sample with peaks corresponding to α-phase Alq(3) in $(0,\overline{1},1)$-orientation 56

42 Sketch of the stacking of Alq(3) molecules in the α-phase for the $(0,\overline{1},0)$-orientation 56
43 Sketch of the stacking of Alq(3) molecules in the α-phase for the (0,0,1)-orientation 57
44 Grazing incidence X-ray diffraction pattern of the $T_{sub} = 165°C$ sample with peaks corresponding to α-phase Alq(3) in $(0,\overline{1},1)$-orientation 58
45 Raman spectra and corresponding optical microscopy pictures at different spots on samples prepared at $T_{sub} = 100°C$ and $T_{sub} = 140°C$. 60
46 Raman spectra and corresponding optical microscopy pictures at different spots on samples prepared at $T_{sub} = 150°C$ 61
47 Raman spectra and corresponding optical microscopy pictures at different spots on samples prepared at $T_{sub} = 173°C$ 62
48 Raman spectra in the phonon region of Alq(3) powders 63
49 Comparison of Raman spectra in the phonon region of a powder, a film and a blank substrate 64

References

[1] C. W. Tang and S. A. VanSlyke. Organic electroluminescent diodes. *Applied Physics Letters*, 51(12):913–915, 1987.

[2] S.Y. Hung, R.L. Kao, K.Y. Lin, C.C. Yang, K.S. Lin, Y.C. Chao, J.S. Wang, J.L. Shen, and K.C. Chiu. Characterization of facial and meridional alq3 thin films fabricated from physical vapor transport at high substrate temperatures. *Materials Chemistry and Physics*, 154:100–106, 2015. ISSN 0254-0584.

[3] M. Brinkmann, G. Gadret, M. Muccini, C. Taliani, N. Masciocchi, and A. Sironi. Correlation between molecular packing and optical properties in different crystalline polymorphs and amorphous thin films of mer-tris (8-hydroxyquinoline) aluminum (iii). *Journal of the American Chemical Society*, 122(21):5147–5157, 2000.

[4] Mario Birkholz. *Thin Film Analysis by X-Ray Scattering*. Wiley-VCH Verlag GmbH & Co. KGaA, 2006. ISBN 9783527607594.

[5] Peter Larkin. *Infrared and Raman Spectroscopy*. Elsevier, Oxford, 2011. ISBN 978-0-12-386984-5.

[6] Sigma-aldrich [online]. URL `http://www.sigmaaldrich.com/catalog/product/aldrich/697737?lang=de&region=AT`.

[7] M. Braun, J. Gmeiner, M. Tzolov, M. Coelle, F. D. Meyer, W. Milius, H. Hillebrecht, O. Wendland, J. U. von Schütz, and W. Brütting. A new crystalline phase of the electroluminescent material tris(8-hydroxyquinoline) aluminum exhibiting blueshifted fluorescence. *The Journal of Chemical Physics*, 114(21): 9625–9632, 2001.

[8] M. Colle, R. E. Dinnebier, and W. Brutting. The structure of the blue luminescent δ-phase of tris(8-hydroxyquinoline)aluminium(iii) (alq3). *Chem. Commun.*, pages 2908–2909, 2002.

[9] M. Muccini, M. A. Loi, K. Kenevey, R. Zamboni, N. Masciocchi, and A. Sironi. Blue luminescence of facial tris (quinolin-8-olato) aluminum (iii) in solution, crystals, and thin films. *Advanced Materials*, 16(11):861–864, 2004.

[10] M. Cölle and W. Brütting. Thermal, structural and photophysical properties of the organic semiconductor alq3. *physica status solidi (a)*, 201(6):1095–1115, 2004. ISSN 1521-396X.

[11] M. Rajeswaran, T. N. Blanton, C. W. Tang, W. C. Lenhart, S. C. Switalski, D. J. Giesen, B. J. Antalek, T. D. Pawlik, D. Y. Kondakov, N. Zumbulyadis, and R. H. Young. Structural, thermal, and spectral characterization of the different crystalline forms of alq3, tris(quinolin-8-olato)aluminum(iii), an electroluminescent material in {OLED} technology. *Polyhedron*, 28(4):835–843, 2009. ISSN 0277-5387.

[12] M.M. Shi, J.J. Lin, Y.W. Shi, M. Ouyang, M. Wang, and H.Z. Chen. Achieving blue luminescence of alq3 through the pull-push effect of the electron-withdrawing and electron-donating substituents. *Materials Chemistry and Physics*, 115(2–3):841–845, 2009. ISSN 0254-0584.

[13] Taiju Tsuboi and Yasuko Torii. Photoluminescence characteristics of green and blue emitting alq3 organic molecules in crystals and thin films. *Journal of Non-Crystalline Solids*, 356(37–40):2066–2069, 2010. ISSN 0022-3093.

[14] I.C. Radu, S. Polosan, I. Enculescu, and H. Iovu. Cathodoluminescence and raman analysis of the finite-size effects in mer-alq3 structure. *Optical Materials*, 35(2):268–273, 2012. ISSN 0925-3467.

[15] University göttingen x-ray generation and computer tomography website [online]. URL `http://www.ph2.physik.uni-goettingen.de/Entdecken_und_Verstehen2.php`.

[16] P. Indelicato L. de Billy E. Lindroth J. Anton J.S. Coursey D.J. Schwab C. Chang R. Sukumar K. Olsen R.D. Deslattes, E.G. Kessler Jr. and R.A. Dragoset. X-ray transition energies (version 1.2). [online], 2005. URL `http://physics.nist.gov/XrayTrans`.

[17] A. Gibaud and G. Vignaud. *Specular Reflectivity from Smooth and Rough Surfaces*, chapter 3, pages 85–131. Springer Berlin Heidelberg, Berlin, Heidelberg, 2009. ISBN 978-3-540-88588-7.

[18] University of reading pplato (promoting physics learning and teaching opportunities) [online]. URL `http://www.met.reading.ac.uk/pplato2/h-flap/phys7_1f_2.png`.

[19] *Ocean Optics* glossary raman [online]. URL `http://oceanoptics.com/glossary/`.

[20] A. Brillante, I. Bilotti, R. G. Della Valle, E. Venuti, M. Mas-Torrent, C. Rovira, and Y. Yamashita. Phase recognition by lattice phonon raman spectra: The triclinic structure of the organic semiconductor dibenzo-tetrathiafulvalene. *Chemical Physics Letters*, 523:74 – 77, 2012. ISSN 0009-2614.

[21] Günter Sauerbrey. Verwendung von schwingquarzen zur wägung dünner schichten und zur mikrowägung. *Zeitschrift für Physik*, 155(2):206–222, 1959. ISSN 0044-3328.

[22] Hyperphysics [online]. URL `http://hyperphysics.phy-astr.gsu.edu/hbase/tables/thrcn.html`.

[23] Harald Spreitzer. Structure and morphology of dioctyloxybenzothienobenzothiophene thin films. Master's thesis, 2016.

[24] L.F. Cheng, L.S. Liao, W.Y. Lai, X.H. Sun, N.B. Wong, C.S. Lee, and S.T. Lee. Effect of deposition rate on the morphology, chemistry and electroluminescence of tris-(8-hydroxyqiunoline) aluminum films. *Chemical Physics Letters*, 319 (3–4):418 – 422, 2000. ISSN 0009-2614.

[25] J.M. Chung, Y.Z. Luo, Z.A. Jian, M.C. Kuo, C.S. Yang, W.C. Chou, and K.C. Chiu. Effects of substrate temperature on the properties of alq 3 amorphous layers prepared by vacuum deposition. *Japanese Journal of Applied Physics*, 43(4R):1631, 2004.

[26] Z.A. Jian, Y.Z. Luo, J.M. Chung, S.J. Tang, M.C. Kuo, J.L. Shen, K.C. Chiu, C.S. Yang, W.C. Chou, C.F. Dai, and J.M. Yeh. Effects of isomeric transformation on characteristics of alq3 amorphous layers prepared by vacuum deposition at various substrate temperatures. *Journal of Applied Physics*, 101(12):123708, 2007.

[27] M. Brinkmann, F. Biscarini, C. Taliani, I. Aiello, and M. Ghedini. Growth of mesoscopic correlated droplet patterns by high-vacuum sublimation. *Phys. Rev. B*, 61:R16339–R16342, Jun 2000.

[28] B. R. Kanchibotla, K. Garre, and D. Aurongzeb. Correlated growth of organic material tris (8-hydroxyquinoline) aluminum (alq3) and its relation to optical properties. *Journal of Applied Physics*, 106(9):096101, 2009.

[29] Grazing-incidence small-angle x-ray scattering community website [online]. URL http://gisaxs.com/index.php/Critical_angle.

[30] Chemie.de lexikon [online]. URL http://www.chemie.de/lexikon/Siliciumdioxid.html.

[31] T. Siegrist, C. Kloc, J. H. Schön, B. Batlogg, R. C. Haddon, S. Berg, and G. A. Thomas. Enhanced physical properties in a pentacene polymorph. *Angewandte Chemie International Edition*, 40(9):1732–1736, 2001. ISSN 1521-3773.

[32] D. S. Qin, D. C. Li, Y. Wang, J. D. Zhang, Z. Y. Xie, G. Wang, L. X. Wang, and D. H. Yan. Effects of the morphologies and structures of light-emitting layers on the performance of organic electroluminescent devices. *Applied Physics Letters*, 78(4):437–439, 2001.

[33] Peter Zaumseil. High-resolution characterization of the forbidden Si 200 and Si 222 reflections. *Journal of Applied Crystallography*, 48(2):528–532, 2015.

[34] C. R. Hubbard, H. E. Swanson, and F. A. Mauer. A silicon powder diffraction standard reference material. *Journal of Applied Crystallography*, 8(1):45–48, 1975.

[35] A. Moser. *Crystal Structure Solution Based on Grazing Incidence X-ray Diffraction: Software Development and Application to Organic Films*. PhD thesis, Graz University of Technology, 2012.

[36] M.H. Wang, T. Konya, M. Yahata, Y. Sawada, A. Kishi, T. Uchida, H. Lei, Y. Hoshi, and L.X. Sun. Thermal change of organic light-emitting alq3 thin films. *Journal of Thermal Analysis and Calorimetry*, 99(1):117–122, 2010. ISSN 1572-8943.

[37] Ralchenko Yu. Reader J. Kramida, A. and NIST ASD Team. Nist atomic spectra database (version 5.4) [online], 2016. URL http://physics.nist.gov/PhysRefData/ASD/lines_form.html.

[38] D. R. Blasini, J. Rivnay, D.-M. Smilgies, J. D. Slinker, S. Flores-Torres, H. D. Abruna, and G. G. Malliaras. Observation of intermediate-range order in a nominally amorphous molecular semiconductor film. *J. Mater. Chem.*, 17:1458–1461, 2007.